

RESEARCH

Open Access



# A semi-empirical scaling model for low-power Hall effect thrusters and its application to the analysis of the Halo thruster performance

Silvia Masillo<sup>1,3\*</sup>, Andrea Lucca Fabris<sup>1</sup> and Paolo Bianco<sup>2,4</sup>

\*Correspondence:

Silvia Masillo  
s.masillo@swissto12.ch

<sup>1</sup>Surrey Space Centre (SSC),  
University of Surrey,  
Guildford GU2 7XH, UK

<sup>2</sup>Airbus Defence and Space,  
Portsmouth PO3 5PU, UK

<sup>3</sup>Present address: Swissto12 SA, Av.  
des Baumettes 19, Renens  
1020, Switzerland

<sup>4</sup>Present address:  
Forschungszentrum Jülich,  
Wilhelm-Johnen-Straße,  
52428 Jülich, Germany

## Abstract

An efficiency breakdown analysis is derived including energy efficiency, propellant utilization efficiency and beam efficiency and correlates the thruster performance with plasma parameters. The methodology can be applied to a partially ionized and multiply-charged discharge plasma. Additionally, a semi-empirical scaling model is introduced, utilizing a novel database of low-power Hall Effect Thrusters to predict performance across various power levels. These models are used to analyze the Halo thruster performance, providing insights into ionization, acceleration, and loss mechanisms. The findings indicate specific performance losses due to plasma-wall interactions, low ionization rate and low mass utilization efficiency and highlight the need to improve the Halo's magnetic field design to enhance thruster performance.

**Keyword** Hall-Effect thruster, Low-power electric propulsion, Semi-empirical model, Performance analysis

## Introduction

The increasing demand for telecommunication services in geosynchronous equatorial orbit (GEO) has been the main driver for the maturation of EP technologies in the 1–5 kW power range since the 1970s [1]. In the last decade, efforts towards lowering the cost of access to space have led to a rapidly increasing interest in small satellites in the low Earth orbit (LEO) and have given further relevance to the advantages that EP systems could deliver. This new space picture has been mostly driven by the fast-growing interest in the commercial market for using LEO telecommunication satellite constellations - which enable low-latency internet access to large parts of the world -, de-orbiting requirements and the possibility of launching as a secondary payload. The common factor behind these scenarios is the additional  $\Delta v$  required to perform maneuvers in LEO. Additionally, thanks to the low thrust and high specific impulse capability, EP allows new maneuvers for longer mission lifetime, continuous operation for drag-compensation and altitude, plane and phase changes.

Despite several EP technologies have already been used on small satellites ( $\sim 500\text{ kg}$ ) as technological demonstrators or as the principal propulsion systems, these systems are still subject of significant research [2]. Since the 1960s, extensive experimental and theoretical studies have provided insights into the physics of plasma thrusters. Yet, their design and development rely on a semi-empirical approach, based on long and expensive flight-qualifying tests on endurance, lifetime, and multi-mode characterization. Progress is being made by integrating simulations and theoretical frameworks with empirical data, although challenges arise from the complex interplay of nonlinear phenomena such as ionization, magnetic confinement, and plasma instabilities. Hall-Effect thrusters (HETs) remain a focal point in EP research due to their high thrust-to-power ratio, efficiency, and extensive flight heritage. Nonetheless, low-power HETs encounter specific challenges, including increased plasma-wall interactions that adversely affect discharge performance and thruster integrity. These issues are compounded by the need for higher plasma density and challenges in generating strong magnetic fields in smaller-scale thrusters. To address these problems, a variety of devices that combine the desirable features of HETs with alternative magnetic field topologies and discharge channel geometries have been proposed. Building upon these considerations, the Halo thruster research project was initiated at Surrey Space Centre, University of Surrey. It aimed to experimentally investigate the physics of a novel low-power electrostatic propulsion system, focusing on utilization efficiencies, ionization and acceleration mechanisms within the thruster discharge channel, and the influence of ground-test facility effects on these properties. The Halo thruster features close similarities to Cusped Field Thrusters (CFTs) and Cylindrical Hall Thrusters (CHTs), but with the addition of a toroidal cusp layer close to the thruster anode which results in magnetic cancellation regions. A hollow cathode neutralizer can be located either externally or internally along the thruster centerline. Ions produced close to anode potential near the Halo were expected to accelerate towards the null point across a strong radial magnetic field barrier. The outgoing ions would then be neutralized at the null point by electrons coming from the neutralizer, as electrons were expected to flow with minimal resistance along the magnetic field lines.

While expanding the range of operating conditions, the prediction of the feasible performance of new thruster designs is also of great interest. In this framework, this paper proposes an analysis based on experimentally-determined plume characteristics and available performance data to build a semi-empirical performance model. Semi-empirical models are based on scaling relations and rely on existing performance measurements to predict how the performance of the propulsion system varies depending on the thruster operating conditions. The overall thruster efficiency can be formulated in terms of multiple efficiency factors and, even though HETs' loss mechanisms are physically coupled, performance loss processes can be mathematically isolated and individually investigated. Several performance methodologies and efficiency factorization techniques have been proposed within the HET community, including the remarkable studies from Komurasaki [3], Kim [4], Morozov and Bugrova [5, 6], Bouchoule and Boeuf [7], Biagioni and Andrenucci [8] and more recent noteworthy works by Linnell and Gallimore [9], Ahedo [10], Hofer [11, 12], Brown [13] and Shagayda [14]. These models have been proven to be very useful in estimating the thruster performance and, over the years, have also been improved to include the effects of beam divergence, multiply charged ions

and neutrals in the jet plume. In this paper, a phenomenological performance model is described in Sec. II. The model does not propose a novel approach, but rather it compares the different studies in the literature to provide a standard methodology which can be applied to a partially ionized and multiply-charged discharge plasma. In Sec. III, a semi-empirical scaling method is introduced. Since semi-empirical models rely on a data library, their main drawback is that their predictive value is limited by the available experimental test results. The method continues and expands the work presented by Shagayda [14] in 2015. Shagayda obtained expressions for predicting the performance of HETs by creating a database of over thirty thrusters which include the Russian SPT (Stationary Plasma Thruster) [15] and KM models [16], the American designs from Busek [17] and NASA [18], the French PPS family by SNECMA Moteurs [19], the Japanese model from MELCOs [20] and the Italian HT from Sitael [21]. Within this work, the database is enlarged by including empirical data from low-power Hall effect-based thrusters tested during the past decade (Sec. IV) and, successively, it is used to forecast the attainable performance of the Halo thruster. Cylindrical Hall thrusters are of particular interest due to performance similarities with the Halo thruster. The Halo thruster experimental data are discussed within this model framework in Sec. A to evaluate the fidelity of the plasma plume measurements in characterizing the thruster performance and improving the understanding of the loss mechanisms.

### Phenomenological performance models

The analysis involves the breakdown of the overall thruster efficiency into various factors, including energy efficiency, propellant utilization efficiency and beam efficiency. The decomposition of the total thruster efficiency in different utilization efficiencies is a way to isolate loss factors and provide means to characterize the conditions that worsen thruster performance in detail.

This model, which combines mostly works from Hofer [11], Goebel [22], Gorshkov [23] and Brown [13], is applicable to a partially-ionized (i.e. < 100% mass utilization) plasma composed of single- and multiply-charge ions, under the hypothesis that all charged particles are accelerated by the same accelerating potential within the discharge channel. These models have been primarily selected as they treat the plasma as composed of multiple species.

The standard performance parameters to describe an EP system are the total thruster efficiency (in Eq. 1), total thruster power (in Eq. 2), total specific impulse (in Eq. 3) and thrust (in Eq. 4) [22]. The use of anode performance parameters makes easier the comparison of thrusters at different stages of development. Hence, in literature, the anode efficiency and anode specific impulse, which considers solely anode parameters, are also widely used.

$$\eta_t = \frac{P_{jet}}{P_t} \quad (1)$$

$$P_t = P_d + P_{EM} + P_{HCN} \quad (2)$$

$$I_{sp,t} = \frac{T}{\dot{m}_t g_0} \quad (3)$$

$$T = \dot{m}_a v_{ex,eq} \approx \sum_k \dot{m}_k \langle v_i \rangle_k \quad (4)$$

The total thrust efficiency is defined as the ratio between the exhaust jet power or kinetic thrust power of the beam,  $P_{jet}$ , and the total power input to the thruster,  $P_t$ , which includes the discharge power,  $P_d$ , the power to generate the magnetic field, if electromagnetic coils are used,  $P_{EM}$ , and any power delivered to the neutralizer or auxiliary system,  $P_{HCN}$ . The analysis is performed at a thruster level, rather than a system level. Therefore, the power delivered to the PPU, flow control system, control and interface units is not considered. The total mass flow rate,  $\dot{m}_t$ , is the sum of the anode flow rate,  $\dot{m}_a$ , and cathode flow rate,  $\dot{m}_c$ . If only anode parameters are used, the anode efficiency is defined as in Eq. 5:

$$\eta_a = \frac{T^2}{2\dot{m}_a P_d} \quad (5)$$

The total specific impulse in Eq. 3 is defined as the thrust per unit weight flow rate of propellant;  $g_0$  is the reference acceleration of gravity equal to  $9.81 \text{ m/s}^2$ . The anode specific impulse is equal to Eq. 6:

$$I_{sp,a} = \frac{T}{\dot{m}_a g_0} \quad (6)$$

In general, the thrust is given by the propellant flow rate times the equivalent exhaust velocity of the propellant,  $v_{ex,eq}$ . In electrostatic thrusters, the thrust is created by different particles ejected from the thruster's discharge channel, including electrons, neutrals and ion species. Because of higher mass and velocity, the momentum flux of ion species highly exceeds electron and neutral ones. Hence, the thrust produced by Hall effect-based thrusters can be described as the sum of the products of the mass flow rate of a certain ion species times the average velocity of the k-th ion species,  $\langle v_i \rangle_k$ . This equation expression does not account for neutral ingestion and beam divergence [22].

The anode efficiency can be factorized into the product of the propellant utilization efficiency,  $\eta_p$ , energy efficiency,  $\eta_E$ , and beam utilization efficiency  $\eta_{div}$ , as in Eq. 7:

$$\eta_a = \eta_P \eta_E \eta_{div} \quad (7)$$

Each of these terms is analyzed in the following sections.

#### A. Propellant utilization efficiency

The propellant utilization efficiency has been analyzed via different approaches in literature.  $\eta_p$  comprises losses linked to nonuniform velocity distribution due to an incomplete ionization, recombination at the walls and the presence of multiple ion species. The term can be factorized into mass utilization efficiency,  $\eta_m$ , charge utilization efficiency,  $\eta_q$ , and neutral-gain parameter,  $\varepsilon_{NG}$ , to align its definition among the models.

According to Hofer and Goebel [22, 24], the thruster mass utilization efficiency quantifies how well the anode propellant is converted into an ion flux. Without taking into account any ingestion from the vacuum facility or the cathode, the anode mass flow rate can be defined as the sum of the flow rates of ionized ( $\dot{m}_b$ ) and unionized propellant ( $\dot{m}_n$ ) as in Eq. 8:

$$\dot{m}_a = \dot{m}_b + \dot{m}_n \quad (8)$$

where the ion beam mass flow rate,  $\dot{m}_b$ , is the sum of the ion species mass flow rates,  $\dot{m}_k$ , and it is related to the ion beam current as in Eq. 9:

$$\dot{m}_b = \sum_k \dot{m}_k = \sum_k \frac{m_{Xe} I_b}{e} \frac{\Omega_k}{Z_k} \quad (9)$$

Here,  $m_{Xe}$  is the mass of the xenon atom,  $e$  is the electron charge,  $I_b$  is the ion beam current calculated as  $I_b = \sum_k I_k$ , where  $I_k$  is the k-th species current,  $\Omega_k$  is the current fraction of the k-th species ( $\Omega_k = I_k / I_b$ ) and  $Z_k$  is the charge-state of the k-th species. Although the study presented herein focuses on xenon as the propellant, the derivation of Eq. 9 is general and applicable to other propellant types, as the efficiency parameters are independent of the specific propellant choice.

The mass utilization efficiency considering a multiply-charged plasma can be evaluated as in Eq. 10:

$$\eta_m \equiv \frac{\dot{m}_b}{\dot{m}_a} = \frac{m_{Xe} I_b}{\dot{m}_a e} \sum_k \frac{\Omega_k}{Z_k} = \frac{m_{Xe} I_b}{\dot{m}_a e} \frac{1}{Q} \quad (10)$$

$\eta_m$  can be calculated using a beam current measurement from a Faraday probe in conjunction with the ion current fractions from a Wien filter or, likewise, using an equivalent ion charge,  $Q$ , as proposed by Brown [13].  $Q$  can be expressed in terms of ion flow fractions ( $\mu_k = \frac{\dot{m}_k}{\sum_k \dot{m}_k}$ ), ion current fractions ( $\Omega_k$ ), and ion species fractions, ( $\zeta_k$ ), as in

Eq. 11:

$$Q = \sum_k \mu_k Z_k = \left( \sum_k \frac{\Omega_k}{Z_k} \right)^{-1} = \frac{\sum_k \zeta_k Z_k^{3/2}}{\sum_k \zeta_k Z_k^{1/2}} \quad (11)$$

$\ddot{\eta}_m$  appears also in other models, such as Gorshkov's one [23], under the different name 'propellant utilization factor'.

In all the models considering a multiply-charged species plasma, the charge utilization efficiency is defined as in Eq. 12:

$$\eta_q \equiv \frac{\left( \sum_k \frac{\Omega_k}{Z_k^{1/2}} \right)^2}{\sum_k \frac{\Omega_k}{Z_k}} = \frac{\left( \sum_k \mu_k Z_k^{1/2} \right)^2}{\sum_k \mu_k Z_k} \quad (12)$$

The charge utilization efficiency is the factor accounting for the presence of multiply-charged ions.

Brown [13] includes in the model the effects of neutrals on the jet velocity distribution. The term in Eq. 13 considers the thrust and energy gained due to the speed of the neutrals and it is greater than unity.

$$\epsilon_{NG} \approx 1 + 2y_0 \frac{1 - \eta_m}{\eta_m \sqrt{Q \eta_q}} \quad (13)$$

where  $y_0$  is the normalized neutral speed that, for example, can be evaluated with the Laser Induced Fluorescence (LIF) technique.

## B. Energy efficiency

The energy efficiency term,  $\eta_E$ , in Eq. 7 takes into account losses due to the ionization process, ohmic heating and radiation that lower the jet kinetic energy. To align the works from Goebel [22], Hofer [24], Gorshkov [23] and Brown [13],  $\eta_E$  can be decomposed into the product of the voltage utilization efficiency and current utilization efficiency.

The voltage utilization efficiency or acceleration efficiency characterizes how effectively the discharge voltage is converted into ion velocity. Theoretically, ions created within the discharge channel are accelerated over a potential drop equal to the discharge voltage to produce thrust. In reality, the acceleration potential is lower, since the plasma potential downstream of the thruster exit is not null and the potential can partially decrease in the discharge channel before the region of maximum ionization. In addition, ions are produced throughout different locations in the discharge channel, therefore they are accelerated at different potential drops.

The models surveyed approximate the ions to be accelerated by the same electrostatic potential. According to Hofer [24], the thruster discharge voltage can be expressed as in Eq. 14:

$$V_d = V_{acc,k} + V_{losses,k} \quad (14)$$

where  $V_{acc,k}$  is the average ion accelerating voltage of the k-th species and the  $V_{losses,k}$  takes into account species-dependent potential losses due to the divergent angle, the non-axial velocity component of the k-th species, and the difference in potential between the discharge voltage and the location where the ion is created. In HETs ions are electrostatically accelerated and their average exit velocity is computed as in Eq. 15, which derives from the conservation of energy expressed in Eq. 16:

$$\langle v_i \rangle_k = \sqrt{\frac{2eV_{acc,k}}{m_{Xe}}} \sqrt{Z_k} = \sqrt{\frac{2e(V_d - V_{losses,k})}{m_{Xe}}} \sqrt{Z_k} \quad (15)$$

$$Z_k e V_{acc,k} = \frac{1}{2} m_{Xe} \langle v_i \rangle_k^2 \quad (16)$$

The voltage utilization efficiency is defined as in Eq. 17:

$$\eta_v \equiv \frac{V_{acc,k}}{V_d} \quad (17)$$

In the model, all ion species are considered to be created across a region of small potential gradient and therefore are subject to the same accelerating voltage, i.e.  $V_{acc,k} \approx V_{acc}$ .

It's worth mentioning that the terminology 'voltage utilization efficiency' can assume different meanings in other literature. For example, in [23], Gorshkov determines the loss factors due to the energy distribution of the ions,  $\gamma_E$ , and the beam angular distribution,  $\gamma_\theta$ , from the measurements of the ion energy and angular distribution in the plasma jet performed with a retarding potential analyzer (RPA). According to this methodology, the voltage utilization efficiency  $\eta_v^*$  is equal to Eq. 18:

$$\eta_v^* = \gamma_E^2 \gamma_\theta^2 \quad (18)$$

Gorshkov's definition of voltage utilization efficiency differs from the other models. This definition can be compared with the plume divergence losses in the beam efficiency introduced by Brown and discussed in Sec. C.

The second term embedded in the energy efficiency is the current utilization efficiency and characterizes how effectively the electrons are used to ionize the propellant.

The discharge current,  $I_d$ , is composed of ion beam current,  $I_b$ , and electron current,  $I_e$ . Applying Kirchoff's Law,  $I_d$  is calculated as in Eq. 19:

$$I_d = I_b + I_e \quad (19)$$

The ion beam current produces thrust; the electron current is used for propellant ionization. By definition, the current utilization efficiency is the fraction of ion beam current relative to the total discharge current,  $I_d$ , as in Eq. 20:

$$\eta_b \equiv \frac{I_b}{I_d} = \frac{e}{I_d m_{Xe}} \sum_k \dot{m}_k Z_k \quad (20)$$

The electron current contributes to propellant ionization, excitation, and ohmic heating due to wall collisions. To improve the design of HETs, the electron current is typically minimized. Nonetheless, there is a practical limit due to the electron current necessary to sustain the discharge. The minimum power required to generate a given ion species can be estimated as in Eq. 21:

$$P_{min} = \frac{e}{m_{Xe}} \sum_k \dot{m}_k Z_k \epsilon_k = I_b \sum \frac{Z_k}{\Omega_k} \epsilon_{b,min} \quad (21)$$

where  $\epsilon_k$  is the ionization potential of k-th ion species (i.e. 12, 33, 65 eV from the neutral ground state for Xe) and  $\epsilon_{b,min}$  is the minimum ionization cost that can also be evaluated as in Eq. 22:

$$\epsilon_{b,min} = \sum_k \mu_k Z_k \epsilon_k \quad (22)$$

The power lost by Joule heating, wall losses and other physical mechanisms is estimated as Eq. 23:

$$P_{loss} = P_d - P_{ion-beam} - P_{min} \quad (23)$$

where  $P_{ionbeam}$  is the power of the ion beam evaluated as the product of the ion beam current,  $I_b$ , and the ion most probable acceleration potential,  $V_{acc}$ .

### C. Beam efficiency

The beam efficiency,  $\eta_{div}$ , is experimentally calculated by taking into account the ion divergence in the plume, which is indicative of the off-axis velocity losses in thrust. To account for a non-unidirectional ion beam, Goebel [22] introduces a correction factor  $F_t$  equal to Eq. 24:

$$F_t = \cos(\theta_{div}) \quad (24)$$

where  $\theta_{div}$  is typically evaluated as the average 95% divergence half-angle of the beam, i.e the half-angle plume divergence which is based on 95% of the beam current. This

formulation has similarities with Gorshkov's losses factor mentioned in Sec. B. Brown characterizes the off-axis cosine losses by considering an effective plume divergence angle,  $\lambda_B$ , which is less than the  $\theta_{div}$ . This is done to reduce errors related to charge exchange (CEX) collisions which artificially increase the measured ion beam current at large plume angles:

$$\eta_{div} = \cos^2(\lambda_B) \quad (25)$$

where  $\lambda_B$  is the far-field divergence angle, that is evaluated from the ratio of the axial beam current,  $I_{Axial}$  and the total ion beam current, as in Eq. 26:

$$\lambda_B = \cos^{-1} \left( \frac{I_{Axial}}{I_b} \right) \quad (26)$$

The axial beam current can be calculated from Faraday probe measurements. Brown mentions that the assumption that the divergence in ion current is representative of the divergence in momentum is only valid if the spatial variation in ion charge species fractions is sufficiently small [13]. The latter can be assessed by angularly resolved measurements using a Wien filter.

#### D. Thruster performance

The main thruster performance parameters can be expressed in terms of utilization efficiencies derived in Sections A to C. This section provides standardized expressions of the performance parameters.

The anode efficiency of the thruster can be expressed as in Eq. 27 [13]:

$$\eta_a = \eta_q \eta_m \eta_b \eta_v \epsilon_{NG} \eta_{div} \quad (27)$$

The thrust and the specific impulse can be formulated as Eqs. 28 and 29 [13], respectively:

$$T = P_d \sqrt{\frac{2m_{Xe}}{eV_d}} \eta_b \sqrt{\eta_q} \sqrt{\eta_m} \sqrt{\eta_v \epsilon_{NG} \eta_{div}} \quad (28)$$

$$I_{sp} = \sqrt{\frac{2eV_d}{m_{Xe} g_0}} \frac{1}{\sqrt{\eta_m} \sqrt{\eta_v \epsilon_{NG} \eta_{div}}} \sqrt{\eta_q} \quad (29)$$

#### Semi-empirical model

The semi-empirical model presented by Shagayda in [14] is based on a homothetic scaling model of the thruster or, in other words, it assumes that all the linear dimensions of the discharge channel change in accordance with the same proportion. Precisely, Shagayda assumes that the discharge channel mean diameter is proportional to the square root of the discharge power (i.e.  $D_T \sim \sqrt{P_d}$ ). To estimate the thruster performance, the utilization efficiencies derived in Sec. A - C are described in terms of the thruster operating conditions and a set of semiempirical expressions are found by comparing the experimental results of a database of around thirty HETs. Precisely, Shagayda demonstrates that for variations of discharge power and voltage, the most significant changes occur in the mass utilization efficiency. The charge utilization efficiency and the ion species fractions have a strong influence on the specific impulse. The current

efficiency and the voltage efficiency do not follow a clear trend when thruster operational points are varied. Following this model:

- the current and the voltage utilization efficiencies are set as constant values based on the experimental data collected in the database;
- the charge utilization efficiency is evaluated from typical values of multiply-charged ion species;
- the mass utilization efficiency is found as a function of the ionization reaction rate,  $\beta_i$ , which is estimated from the electron temperature (dependent on the specific operating conditions) and ionization cross-section;
- the anode efficiency is evaluated as in Eq. 30:

$$\eta_a = \eta_v^* \eta_b \eta_q \eta_m \quad (30)$$

here  $\eta_v^*$  is defined as in Eq. 18,  $\eta_b$  as in Eq. 20,  $\eta_q$  as in Eq. 12 and  $\eta_m$  is derived from the following interpolation of empirical data:

$$\eta_m = (1 - \exp(-C_2 Q_2)) = \left(1 - \exp\left(-C_2 \frac{m_{Xe} \beta_i \sqrt{P_d}}{\sum Z \mu_k V_d}\right)\right) \quad (31)$$

where  $C_2$  is a constant found by minimizing the standard deviation of Eq. 30 and the anode efficiency empirical data. The dimensions of  $C_2$  are  $(V \cdot s)/(m^3 \sqrt{W})$ .

The predicted thrust and anode specific impulse can be also evaluated as a function of the discharge power and discharge voltage according to Eqs. 28 - 29 in Sec. D.

Shagayda's database of experimental data lacks a sufficient number of experimental results from low-power HETs to capture the performance of the Halo thruster and low-power Hall effect-based thrusters in general. In the following section, a new set of data is compiled and, following similar assumptions to Shagayda's semi-empirical model, empirical coefficients are evaluated to enable the prediction of low-power conventional and innovative HET designs.

#### A. Low-power Hall effect based thruster data

The dataset used within this work includes commercial and laboratory models of Hall-based thrusters working at power levels lower than 1 kW and using xenon as propellant. The library contains around 60 thrusters, including novel HET configurations such as CHTs, CFTs and magnetically shielded HETs. The thrusters are listed in Table A in the Appendix. From the Russian literature, data are extracted for the KM-20 [25], KM-32, KM-45, KM-60 [26, 27], SPT-30 [28],  $\alpha - 40$  SPT [25], SPT-50 and SPT-70 [29], T40 HTC [30], Plas-34 and Plas-40 by Fakel [31], D-38 and T-27 by TSNIIMASH [32, 33]. From the US, the following EP systems have been included: the BHT-100 [34], BHT-200 [35, 36], BHT-600 [37] and BHT-1000 [38] by Busek, MaSMI-40 and MaSMI-60 (Magnetically Shielded Miniature Hall thruster) [39, 40] by NASA, the micro HET [41] and the Z70 [42] developed at Stanford University, the Aurora HET by Orbion Space Technology [43], the ACE by Astra [44], the Halo by Exoterra [45], the Mini SPT [32] and DCFT [46] designed at MIT, the CHT models studied at PPPL [47–50]. Moreover, the database includes the OEFT (Outside Electric Field Thruster) [51], CAM200 [52] and CAMILA (co-axial magneto-isolated longitudinal anode) [53] by the Asher Space

Research Institute (ASRI), the NCHT (Narrow Channel Hall Thruster) [54], IHET-300, the R-200 and R-800 thrusters [55] by Rafael, Israel, the HEET by LAJP, SPT-20 M, ST-25 and ST-40 [56] by SETS (Space Electric Thruster Systems), the SHT 100 and SHT 250 by Seran, Ukraine, the ISCT-100 [57], ISCT-200-US and ISCT-200-MS [58] by CNRS and the ExoMG<sup>TM</sup> by ExoTrail [59], France, the HT100 by Alta [60], Italy, the CHTs, 50 W-class, 300 W-class annular HETs [61–63] and the KCHT-50 and KmCht50 [64, 65] by KAIST, Korea, the 100 W-class HET by JAXA [66, 67], the CHTs, TCHT-3A, TCHT-3B and TCHT-4 from Osaka University [68, 69], Japan, the MUSIC (Multistage Ignition Compact thruster) by Alienia [70], Singapore, the CHTs [71–73] from Harbin Institute of Technology, China and the HEMPT developed at Thales Germany GmbH [74].

Comparisons of the thrust, anode specific impulse and anode efficiency of the EP systems included in the database are plotted in Fig. 1. It is important to note that AHTs, CHTs, and CFTs exhibit distinct performance characteristics and are at different stages of technological maturity. Although alternative Hall-effect-based configurations may offer advantages such as extended thruster lifetime, they typically demonstrate lower performance compared to conventional AHTs. The Hall thruster design in the mid-high power range (1 - 10 kW) has reached quite a mature knowledge, while the scaling-down of this technology is still characterized by unsolved challenges. This justifies the dispersion observed in the graphs, which reflects the lack of an ideal scaling law for low-power HETs. The top graph in Fig. 1 highlights a linear relationship between thrust and anode discharge power. The graph in the middle shows how the anode specific impulse increases rapidly between a few tens to around 200 W, then it reaches a plateau. A similar trend is observed in the bottom graph of Fig. 1 which displays the anode efficiency. Most of the thrusters show efficiency in the 20–40% range for power levels higher than 200 W and quite a broad dispersion is observed at lower power. The semi-empirical model, here presented, is based on a set of experimental data which are quite spread. Additionally, especially in the case of the anode efficiency, the absence of a clear functional relationship suggests that there may be non-linear trends that the model is unable to capture. In order to assess the goodness-of-fit between the semi-empirical model and the data, the estimate of  $C_2$  in Eq. 31 is found by maximizing the  $R^2$  value as further explained in Sec. B.

## B. Model refinement

As defined in Eq. 27, the anode efficiency can be evaluated as the product of utilization efficiencies. The core of the semi-empirical model is to define values of the utilization efficiencies in accordance with the empirical data of the dataset.

Typical current utilization values for the thrusters here surveyed range between 0.48 and 0.74. There is not a clear trend between the empirical data of  $\eta_b$  and the thruster operative conditions, therefore the assumption that  $\eta_b$  is related to the design rather than the thruster nominal working points is considered. A first attempt is performed by taking the average value of  $\eta_b = 0.62$  as a constant for the following calculations.

Similarly, the voltage utilization efficiency spans between 0.73 and 0.92 and there is not a clear correlation between  $\eta_v^*$  and the thruster discharge power and voltage. The average value  $\eta_v^* = 0.82$  is used in the semi-empirical model.

To evaluate the charge utilization efficiency, the relation between empirical data of the ion species fractions and thruster discharge power is analyzed. The reference model

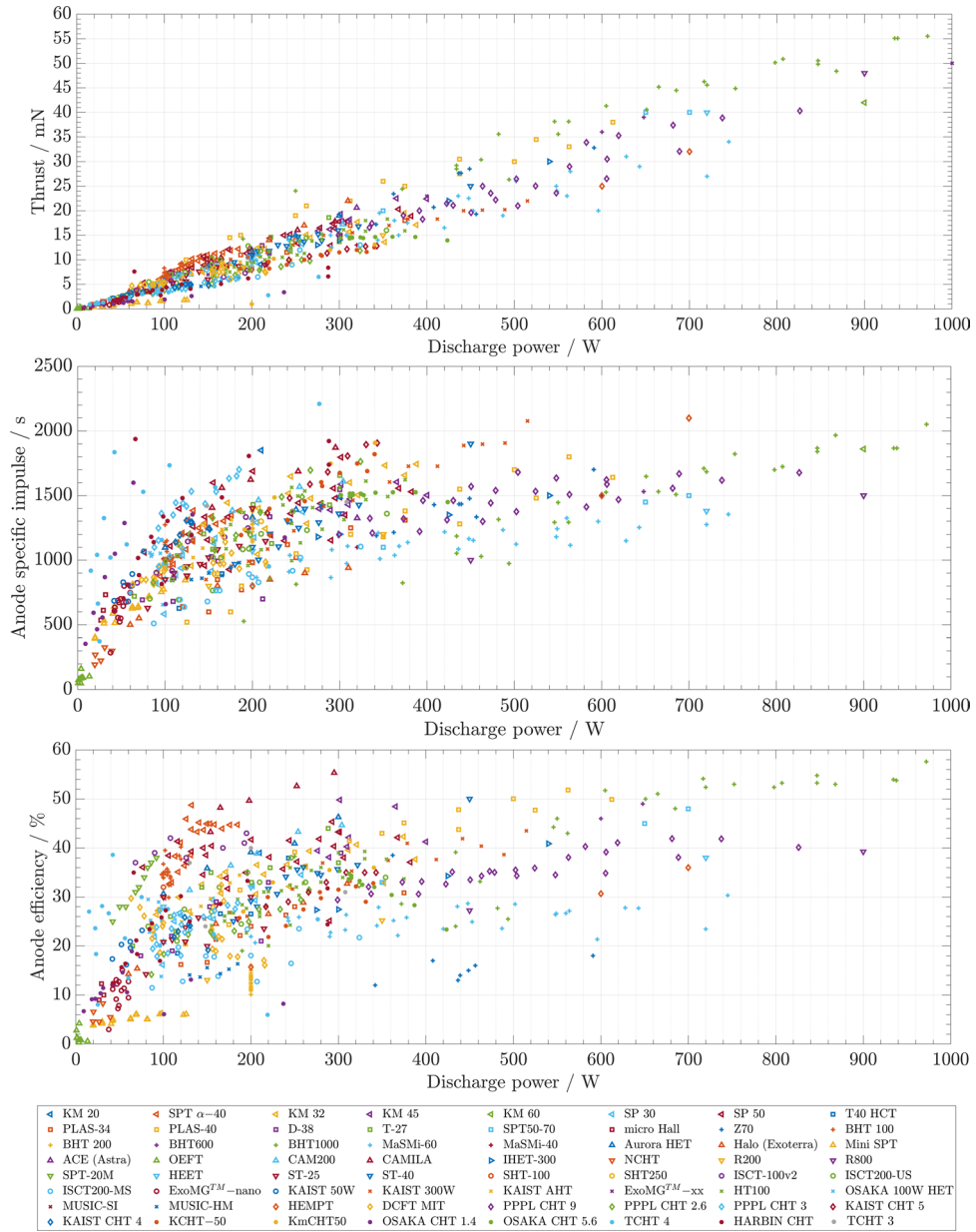


**Fig. 1** Dataset comprising < 1 kW hall effect based thrusters. Performance is plotted as a function of the discharge power. On the top: thrust as function of the discharge power; in the middle: anode specific impulse as function of the discharge power; on the bottom: anode efficiency as function of the discharge power. The references numbers of the sources of data for each thruster are reported in the text of Sec. A

developed by Shagayda [14] is based on experimental data from a single thruster: the conventional Hall thruster NASA-173Mv2 working in optimized operative conditions [75]. The ion species are assumed to be dependent on the discharge voltage and are approximated by linear relations. This approach is modified in the present study to include data from multiple thrusters. Data are collected from conventional HETs (BHT 200, BHT 600, OSAKA 100 W), MS-HETs (MaSMi-40 and MaSMi-60) and CHTs (KAIST 50W, KCHT-50, KmCHT50) working at a power level below 1kW and plotted in Fig. 2. In comparison to unshielded annular HETs, CHTs and MS HETs feature higher multiply-charged ion current fractions. The higher proportion in MS-HET is usually

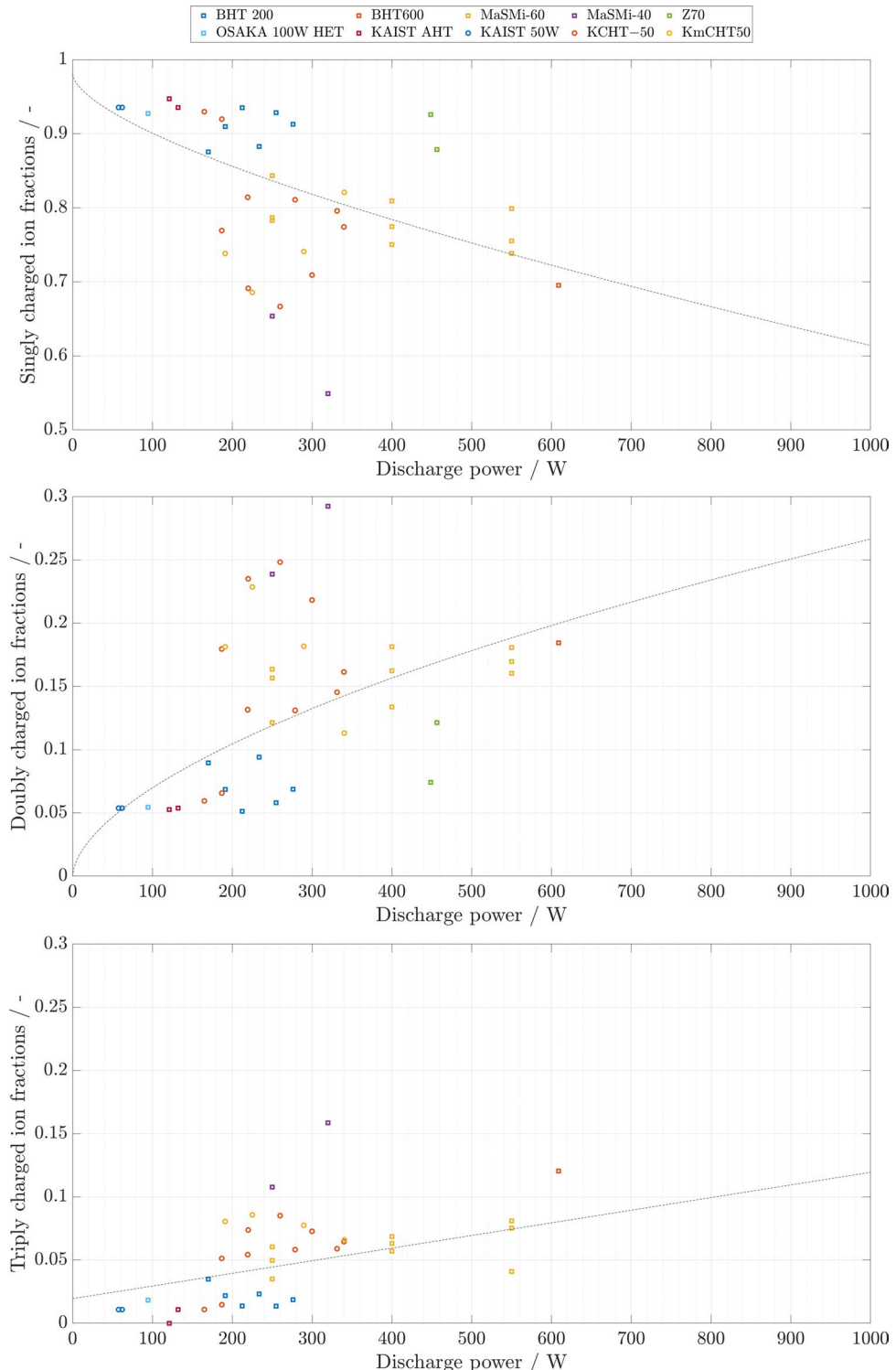


**Fig. 2** The ion species mass flow fractions mapped as a function of the discharge power. Empirical data are collected from annular het (BHT 200, BHT 600, OSAKA 100 W, Z70), magnetically shielded het (MaSMi-40 and MaSMi-60) and CHTs (KAIST 50W, KCHT-50, KmCHT50). The fitting curves of the experimental data (in Eqs. 32 - 34) are plotted as dashed lines. The references numbers of the sources of data for each thruster are reported in the text of Sec. A

explained by the higher electron temperature recorded in these EP devices due to the reduced electron cooling at the walls. Regarding CHTs, the hypothesis that converging ion beams in the thruster increase the plasma potential on the central axis and lengthen the residence time of slow ions in the discharge channel is a possible explanation for the higher population of multiply charged species. Considering ion species fractions from a typical HET only would, in consequence, overestimate the singly charged ion fractions and underestimate higher-charged ion fractions.

Therefore, the present study aims to fit a model to experimental data characterized by a considerable degree of variability and lacking a clear functional relationship. This pronounced variability is related to the fact that data are obtained from thrusters characterized by dissimilar designs and at different development stages. The goodness-of-fit between the model and the data is assessed by maximizing the R-value, a widely-used measure of the strength of the linear association between the variables. However, it is essential to recognize that the R-value remains low and acknowledge the limitations of this model and cautiously interpret the findings. These limitations entail that the model may have limited predictive power and may not adequately discern crucial patterns in the data. However, expanding the analysis to encompass a broader range of experimental data than the reference model [14] can aid in predicting the fractions of multiply-charged ions for a model that aims to incorporate various thruster designs at low power levels. Taking into account the literature data surveyed in this study, the doubly-charged fractions increase exponentially, while the triply-charged fractions increase linearly with power. The fraction of singly-charged ions can be estimated by calculating the difference between the two other species. The analysis does not consider ion species with fractions lower than 0.005, so higher-charged ion species are not included. These relations, expressed in Eqs. 32 to 34, minimize the data standard deviation and are the best fitting for the set of data here analyzed. The limitations of the fitting model highlight the need to expand the database of empirical information for emerging low-power Hall-type propulsion technologies. This underscores the importance of gathering a more extensive collection of empirical data to facilitate the development of accurate models for predicting the performance of these novel propulsion systems. In addition, considering a single thruster category, e.g. annular HET, CHT or CFT, would enhance data coherence and reduce dispersion. Such an approach will improve the reliability of predictions and enable a more comprehensive evaluation of the performance of low-power Hall-type propulsion technologies.

The ion mass flow fractions can be approximated as:

$$\mu_{Xe^+} = 1 - \mu_{Xe^{2+}} - \mu_{Xe^{3+}} \quad (32)$$

$$\mu_{Xe^{2+}} = \Gamma_{Xe^{2+}} \cdot P_d^{0.5815} \quad (33)$$

$$\mu_{Xe^{3+}} = \Gamma_{Xe^{3+}} \cdot P_d + 0.0194 \quad (34)$$

where  $\Gamma_{Xe^{2+}}$  and  $\Gamma_{Xe^{3+}}$  are dimensional constants. Their values are  $\Gamma_{Xe^{2+}} = 0.0048 \text{ W}^{-0.5815}$  and  $\Gamma_{Xe^{3+}} = 0.0001 \text{ W}^{-1}$ .

Given the ion mass flow fractions, the predicted charge utilization efficiency,  $\eta_q$ , and the predicted value of  $\sum_k \sqrt{Z} \mu_k$  are calculated as in Eq. 12 and plotted as a function of

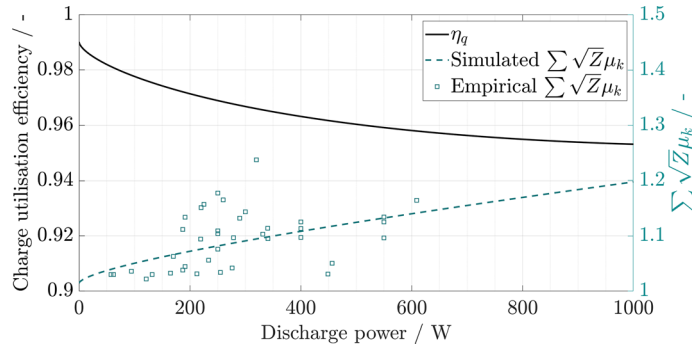


**Fig. 3** Charge utilisation efficiency and simulated and empirical values of  $\sum_k \sqrt{Z} \mu_k$  as a function of the discharge power. The charge utilisation efficiency is evaluated as in Eq. 12, considering the ion species mass flow fractions evaluated as in Eqs 32 - 34

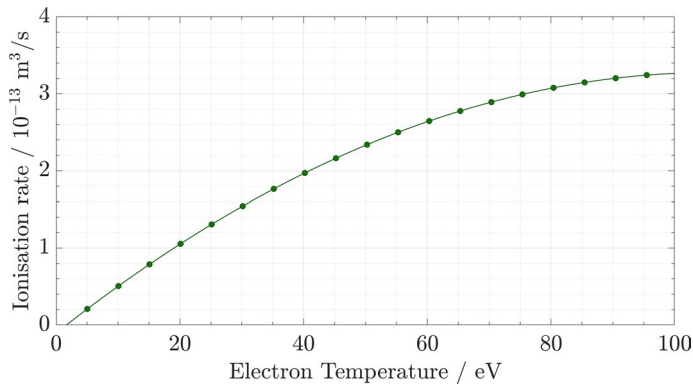


**Fig. 4** Ionization rate evaluated in [77] as function of the electron temperature

the discharge power in Fig. 3. The empirical values of  $\sum_k \sqrt{Z} \mu_k$  are also plotted in Fig. 3 to confirm the dependence of the ion mass flow fractions on the discharge power.

The mass utilization efficiency is the last figure of merit to be calculated. Shagayda demonstrates that the mass utilization efficiency depends mainly on the potential drop in the ionization region, the thermal state of the thruster and the ionization reaction rate (see Eq. 31). Experimental data [24, 76] show that the voltage loss in the ionization zone is almost constant and independent of the thruster operating modes. The ionization rate,  $\beta_i$ , is calculated as a function of the electron temperature  $T_e$  (eV) (see Fig. 4) by assuming a Maxwellian electron velocity distribution function [77].

Finally, the electron temperature is assumed proportional to the discharge voltage in the form [78, 79]:

$$T_e = C_{T_e} \cdot V_d \quad (35)$$

The coefficient  $C_{T_e}$  is evaluated by comparing the operative conditions in which the mass utilization efficiency should be maximum. These conditions are reached at the discharge voltage for which the ratio of the anode efficiency and the charge utilization efficiency is maximum - according to Eq. 27 for constant values of  $\eta_b$  and  $\eta_v^*$  - and at the electron temperature for which the ionization rate to electron temperature ratio reaches its upper limit. The latter is numerically computed and it is equal to  $T_e = 23.9 \text{ eV}$

for xenon [14]. By comparison of the empirical results of the database, the first condition is satisfied around 300 - 340 V. The coefficient  $C_{T_e}$  is therefore assumed equal to 0.07.

Given the anode efficiency expression in Eq. 30 and the mass utilization efficiency relation in Eq. 31, the last coefficient to evaluate is the dimensional constant  $C_2$ . The empirical anode efficiency values are plotted as a function of the parameter  $Q_2$  (see Eq. 31) in Fig. 5. The estimate of  $C_2$  is found by minimizing the standard deviation of the experimental points from the estimate of the anode efficiency described as in Eq. 30. The solid line curve in Fig. 5 is found for  $C_2 = 1.7406 \cdot 10^{12} (V \cdot s)/(m^3 \sqrt{W})$ . The experimental data in Fig. 5 include points from HETs and CFTs (empty circles) and CHTs (empty squares).

### Model results and discussion

The semi-empirical model results are here presented. The results are obtained for  $\eta_b = 0.62$ ,  $\eta_v^* = 0.82$ ,  $\eta_q$  computed from the ion flow fractions expressed as in Eqs. 32 - 34,  $\eta_m$  calculated as in Eq. 31, where  $C_2 = 1.7406 \cdot 10^{12} (V \cdot s)/(m^3 \sqrt{W})$  and the ionization rate  $\beta_i$  estimated as a function of the electron temperature. The empirical coefficients are obtained based on a database of around 60 thrusters, including conventional HETs, MS-HETs, CFTs and CHTs, working at power levels up to 1 kW and using xenon as propellant. The estimated performance of the thrusters is summarized in the diagram in Figs. 6 and 7. The performance diagrams illustrate the predicted anode specific impulse as a function of the predicted thrust and the predicted anode specific impulse as a function of the predicted anode efficiency. The anode efficiency, anode specific impulse and thrust are evaluated, respectively, as in Eqs. 30, 29 and 28, by making explicit the dependence of  $\eta_m$  on  $C_2$  and  $Q_2$  as expressed in Eq. 31. The plots are the superimposition of two sets of curves: one group corresponds to a change in the discharge voltage for fixed values of discharge power ranging between 100 W and 1000 W; the other group compares the change in discharge power for fixed discharge voltage data spanning from 100 V to 1000 V. The discharge voltage and power values are shown close to the curves. Empirical data from Fig. 1 are also added to the plots (empty markers). By specifying the input power and voltage of the thruster, the anode specific impulse and the thrust can be estimated from the performance diagram in Fig. 6. In the same way, the anode specific impulse and the anode efficiency can be predicted from Fig. 7. Or else, if some

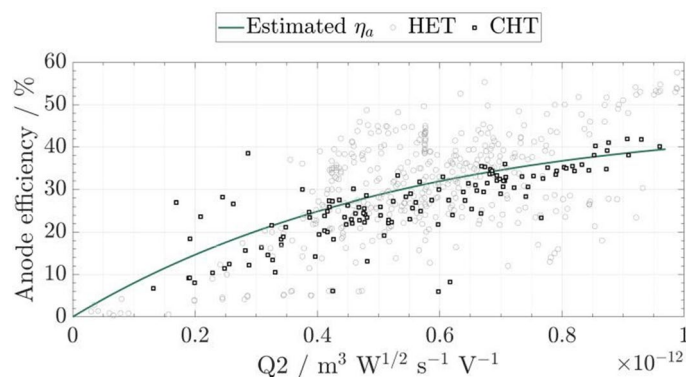


**Fig. 5** Empirical anode efficiency values as a function of the parameter  $Q_2$  in Eq. 31. The experimental points refer to HETs and CFTs (empty circles) and CHTs (empty squares). The estimate of the anode efficiency is plotted as a solid line according to Eq. 30 for  $C_2 = 1.7406 \cdot 10^{12} (V \cdot s)/(m^3 \sqrt{W})$

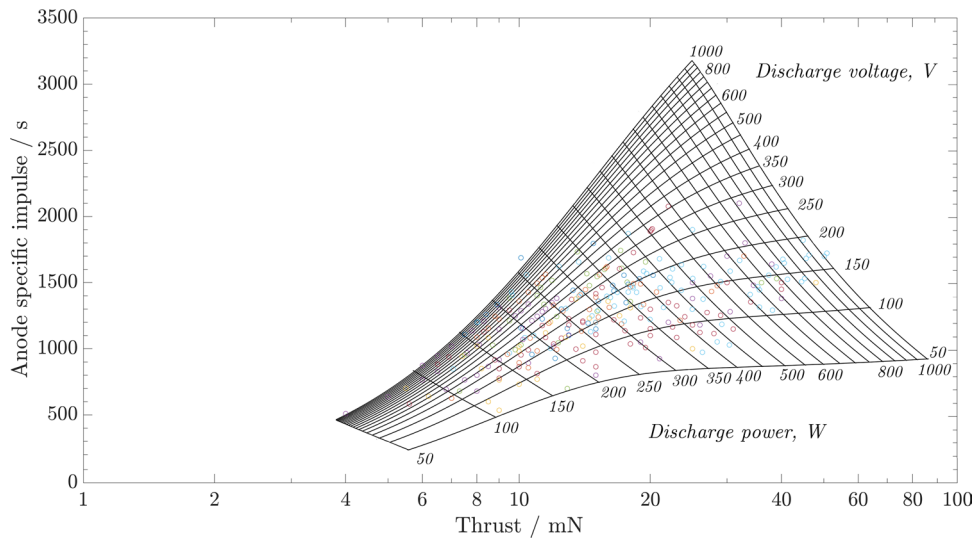


**Fig. 6** Estimated anode specific impulse as a function of the thrust at different discharge powers and discharge voltages. Empirical data from Fig. 1 are plotted with empty markers. Each thruster's operating range is listed in Table 1 in Appendix

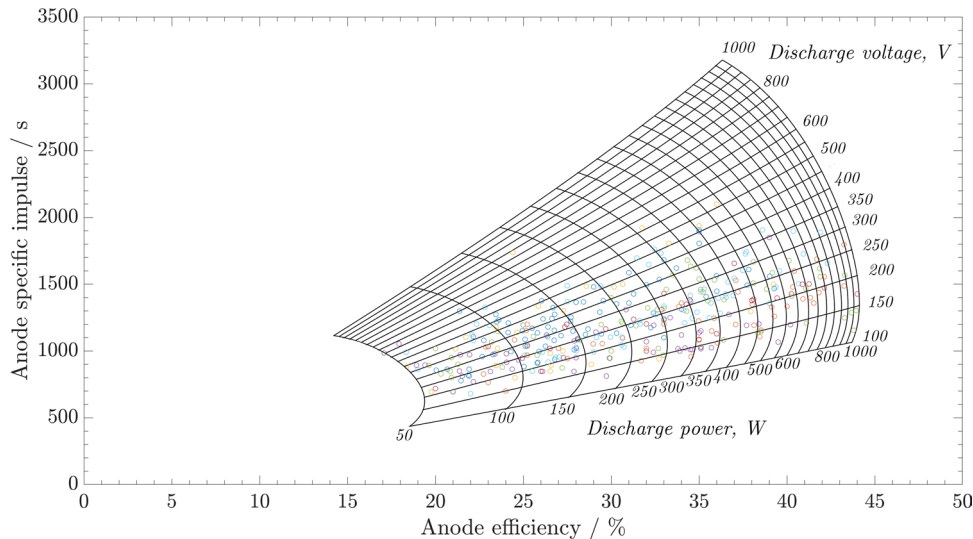


**Fig. 7** Estimated anode specific impulse as a function of the anode efficiency at different discharge powers and discharge voltages. Empirical data from Fig. 1 are plotted with empty markers. Each thruster's operating range is listed in Table 1 in Appendix

performance values are used as input requirements, the plots are useful to determine the range of power level and the discharge voltage necessary to reach those requirements.

As already mentioned, the semi-empirical model here discussed is a refinement of Shagayda's methodology in [14]. The databases on which the models are based are quite dissimilar (i.e. only five thrusters from Shagayda's database could be included in the library presented in Sec. A), since they are focusing on different thruster categories. While Shagayda includes HETs at a TRL 7 or above working at discharge power levels up to 10 kW, this work aims to predict performance levels of innovative HET designs. Consequently, the semi-empirical coefficients are found over a much more dispersive

dataset, which reflects the difficulties in operating Hall-based thrusters at low power levels and the multitude of solutions worldwide researched.

Comparing the two methods, one can speculate on the main dissimilarities between HETs working in the mid-high power range and Hall-based thrusters operating at a power level lower than 1 kW.

The current utilization efficiency,  $\eta_b$ , used in Shagayda's model is equal to 0.8 while, based on the empirical data here surveyed, an average value of  $\eta_b$  is estimated to be 0.62. Decreasing the size of the thrusters has a direct consequence on the confinement of the electrons in the discharge channel and reduces the effectiveness of the electrons in ionizing the propellant. Lower  $\eta_b$  is indeed caused by higher electron current in the discharge plasma. Novel thruster designs such as CHTs and CFTs are advantageous in terms of reducing losses to the wall but are not impactful in improving current utilization efficiency.

The voltage utilization efficiency,  $\eta_v^*$ , shares the same value between this work and Shagayda's model. In other words, the combination of potential losses in acceleration voltage and in beam divergence is similar for various HET designs.

To predict the charge utilization efficiency,  $\eta_q$ , Shagayda's found a relationship between multiply-charged species and discharge voltage based on the data measured in the NASA-173Mv2 thruster [80]. Comparing different HET designs in the mid-low power regime has here proven a much clearer relation between fractions of multiply charged ions and thruster power levels. In general, HETs working below 1 kW show greater fractions of higher-charged species and, in novel designs such as CHTs and MS-HET, this finding is even more evident. To account for  $\eta_q$  effects, it has been assumed that the doubly charged ion fractions increase as a power function for increasing power levels and the rise of triply charged ion fractions is linear. These functions are found by minimizing the standard deviation between the empirical data collected for different thruster designs and the data trendline. The estimation of the mass utilization efficiency,  $\eta_m$ , is ultimately related to the electron temperature in the ionization region. Following literature studies, the electron temperature is evaluated as a function of the discharge voltage as in Eq. 35. The value of  $C_{T_e}$  found by Raitses comparing different Hall thruster configurations in [79] is equal to 0.1. Dannenmayer [78] derived a similar expression in which  $C_{T_e}$  is around 0.12. Finally, the coefficient used by Shagayda is 0.044 and it is derived by comparing the electron temperature and the empirical discharge voltage for points at which the mass utilization efficiency reaches its maximum. A similar procedure is used within this work and  $C_{T_e}$  is set equal to 0.077. Shagayda estimates  $C_{T_e}$  taking into account the uncertainties associated with the dependence of the multiply-charged ion fractions on the discharge voltage, which lower the electron temperature at which the anode efficiency is maximum of around 11–13%. This uncertainty has not been considered in the present work, since a correlation between multiply-charged ions and discharge voltage has not been found from the empirical data.

### The Halo thruster

The Halo thruster was originally developed at the Surrey Space Centre (SSC), University of Surrey, in 2010 and investigated by a consortium comprising SSC, Surrey Satellite Technology Ltd. (SSTL), Airbus Defense and Space, and Imperial College London. The thruster's main components, as shown in Fig. 8, include a boron nitride (BN) cylindrical

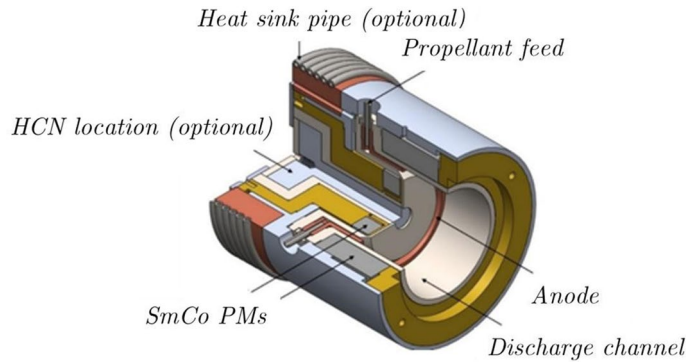


**Fig. 8** A cutaway view of the Halo thruster 3D CAD

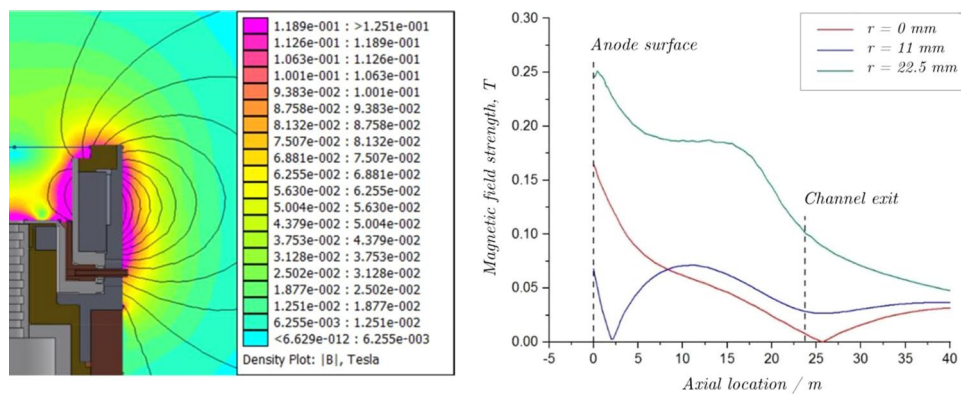


**Fig. 9** PM Halo thruster B-field circuit model simulated by FEMM [81] and B-field strength profile. On the right-hand-side, the plot shows the B-field strength profile as a comparison between the symmetry axis of the thruster ( $r=0$  mm - red line), the axial path intersecting the Halo ( $r=11$  mm - blue line), the axial path starting at the downstream surface of the anode ( $r=22.5$  mm - green line)

discharge channel, a positively biased copper anode that also serves as a xenon propellant distributor, propellant lines, a copper heat sink, permanent magnets (PMs), and the HCN. The magnetic field generated by samarium cobalt (SmCo) PMs creates a cusped magnetic topology featuring field cancellation regions, where the magnetic field strength drops to zero. The Halo thruster's magnetic field is designed with a null point along the discharge channel centerline and an annular “halo” near the anode. The B-field flux density, calculated by Finite Element Method Magnetics (FEMM) [81], is shown in Fig. 9. The figure highlights an annular magnetic field cancellation region within the discharge channel enclosed by a toroidal cusp structure along with a spherical magnetic field cancellation region, which is also enclosed by a cusp structure, along the thruster axis of symmetry downstream of the thruster exit. The Halo is located approximately 5 mm in front of the inner magnet. The B-field strength reaches its maximum along the discharge channel walls where it increases above 0.2 T. On the right-hand-side of Fig. 9, the plot shows the B-field strength profile as a comparison between the symmetry axis of the thruster ( $r=0$  mm - red line), the axial path intersecting the Halo ( $r=11$  mm - blue line), the axial path starting at the downstream surface of the anode ( $r=22.5$  mm - green line) [82]. The back plate of the cylindrical discharge channel features a 13 mm diameter cavity which enables the testing of Halo with a centrally-mounted cathode configuration. In this configuration, the cavity serves as a corridor for the electrons emitted by

the neutralizer, as these are created upstream of the anode plate and are attracted by the positive bias. In the conventional externally-located cathode configuration, a BN or molybdenum section is normally used to close the central cavity (Fig. 8). The characterization of the Halo thruster was based on the experimental apparatus described in [83–85].

#### A. Efficiency analysis of the Halo thruster

In this section, the Halo thruster efficiency is analyzed in terms of multiple utilization efficiencies characterizing the physical processes that contribute to the generation of useful thrust. The efficiency breakdown analysis follows the methodology described in Sec. II and uses plasma properties derived from the following diagnostic probes:

- a Faraday probe outputs are used for the evaluation of the beam utilization ( $\eta_{div}$ ) and current utilization ( $\eta_b$ ) efficiencies;
- a Wien filter is used to measure the parameters needed to calculate the charge utilization ( $\eta_q$ ) and voltage utilization ( $\eta_v$ ) efficiencies;
- combined measurements from the Faraday probe and the Wien filter are used to determine the mass utilization efficiency ( $\eta_m$ ) and neutral-gain parameter ( $\varepsilon_{NG}$ ).

The accuracy of the measurements obtained with the Faraday probe and the Wien filter is discussed in detail in [85]. In particular, the Faraday probe data are corrected for the following:

- Errors due to secondary electron emission (SEE) from the probe surface and the collection of low-energy ions by the collector side walls;
- Systematic errors in the coordinate system used for measurements;
- Sheath edge effects on the negatively biased collector;
- Facility-induced effects;
- Misalignment errors.

Errors affecting the Wien filter measurements—such as probe misalignment, uncertainties in the data acquisition system, sensitivity to background pressure, ion losses due to CEX collisions, and inaccuracies in ion velocity measurements caused by particle accumulation and collisions within the probe - are also discussed in [85]. Additionally, uncertainties related to the electronic measurement system are taken into account.

Trends in the Halo thruster's performance, specific impulse and efficiency are obtained for the thruster coupled with a newly designed HCN - described in [86] -, which can be positioned externally to the thruster or internally along the thruster centerline. These configurations are named 'Ex-Halo', if the HCN is externally mounted, and 'Int-Halo' if the HCN is centrally-located. The two Halo thruster configurations are characterized in terms of ion beam current density, multiply-charged ion fractions, discharge oscillations and electron temperature, allowing the basic physics of operation of the devices to be inferred and compared [85]. The operative conditions, here listed, are selected to operate the thruster within adequate thermal margins, howbeit proving reasonable performance and stability:

- The HCN and the thruster are electrically isolated from the vacuum chamber and kept floating during measurements;

- High-purity xenon gas is used as the propellant for both the anode and the hollow cathode;
- The HCN has a nominal xenon mass flow rate of  $\sim 0.1$  mg/s. After ignition, the cathode keeper current is kept constant at 2.5 A, the cathode heater is off;
- For Ex-Halo, the thruster anode potential ranges between 150 and 350 V;
- For Ex-Halo, the anode mass flow rate ranges between 0.98 mg/s and 1.97 mg/s;
- For Int-Halo, the anode mass flow rate ranges between 0.49 mg/s and 0.98 mg/s;
- For Int-Halo, the thruster anode potential range depends on the mass flow rate. Overall, data between 100 and 300 V are documented. Nevertheless, repeatable results are only obtained between 150 and 250 V at 0.49 mg/s, between 100 and 200 V at 0.74 mg/s and 0.98 mg/s;
- Tests are performed at a background pressure between  $1 \times 10^{-5}$  Torr and  $5 \times 10^{-5}$  Torr (not corrected for xenon).

Before the experiments, the thruster is exposed to vacuum conditions for around 12 hours to allow for the outgassing of the components. Subsequently, a procedure for baking out and activating the thermionic emitter of the HCN is performed. To let the thruster reach a steady-state condition, the discharge is ignited for around 15–30 minutes before plasma diagnostics data are recorded. It should be noted that the comparison between the Int-Halo and Ex-Halo configurations is constrained by their differing stable operating regimes, as thermal limitations in the Int-Halo prevented operation under the same conditions as the Ex-Halo.

The I-V characteristics obtained with the Ex-Halo and Int-Halo are shown in Figs. 10 and 11. The curves are evaluated at three different xenon mass flows. The Halo I-V characteristics show similar behavior to conventional HETs [22]. At a given discharge voltage and propellant flow rate, the discharge current and, consequently, the input power in the Int-Halo thruster, are both larger than the data recorded for the Halo thruster in the externally-located HCN configuration.

The Ex-Halo thruster features a thrust level between 2 and 25 mN, an anode specific impulse between 150 and 1400 s and an anode efficiency between 2 and 21%, depending on the input power (the power range surveyed is  $< 1$  kW). The Int-Halo thruster

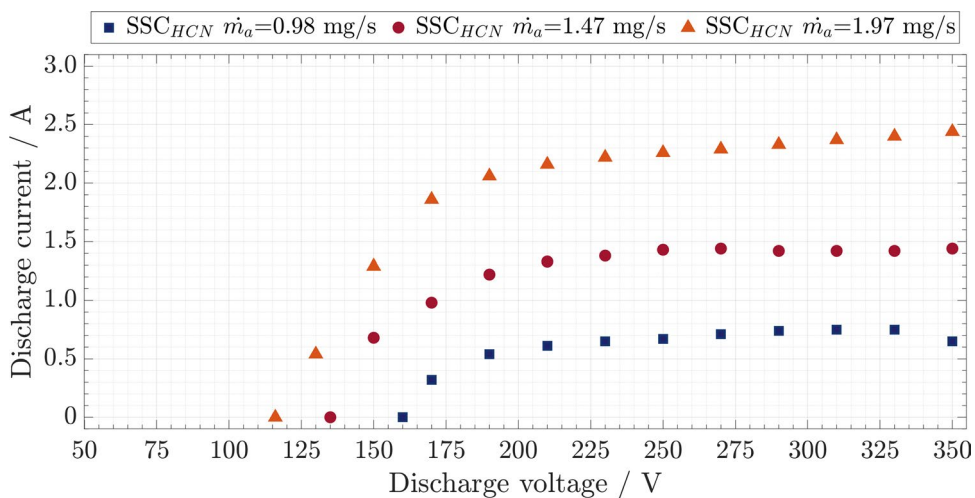


**Fig. 10** Externally located HCN Halo thruster configuration current-voltage characteristics for 0.98, 1.47 and 1.97 mg/s xenon flow rates to the anode

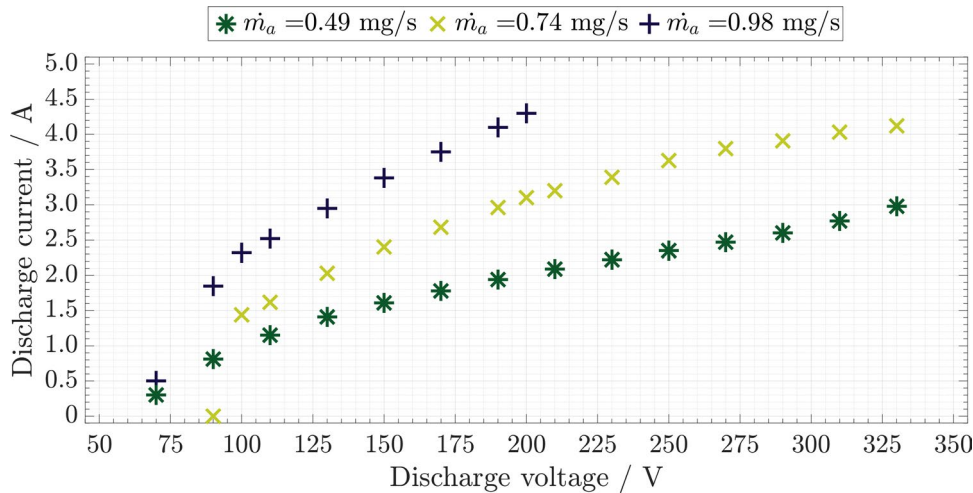


**Fig. 11** Internally located HCN Halo thruster configuration current-voltage characteristics for 0.98, 1.47 and 1.97 mg/s xenon flow rates to the anode

demonstrates thrust levels in the 3–10 mN range, an anode specific impulse between 650 and 1070 s and an anode efficiency between 3 and 7%, depending on the input power.

The analysis of the utilization efficiencies has emphasized that, in general, the Halo thruster's performance is lower in comparison to existing CHTs and CFTs, as the magnetic cusps and the B-field null regions do not have a strong local confining influence on the plasma, with significant wall losses and enhanced electron current collected to the anode, resulting in low mass and current utilization efficiencies:

- The Ex-Halo demonstrates low values of mass utilization efficiency ( $\eta_m$ ) in the low-voltage range (150 V – 200 V) and at all the mass flow rates surveyed, demonstrating that a large fraction of propellant injected through the anode is not ionised. Between 250 V – 350 V,  $\eta_m$  presents higher values, ranging from 0.55 to 0.9;
- The Ex-Halo shows an increase of current utilization efficiency ( $\eta_b = 0.4 - 0.9$ ) with increasing discharge voltage, which can be attributed to an increase of multiply-charged ions or in some cases, to the decrease of the electron current;
- The Ex-Halo features a charge utilization efficiency ( $\eta_q$ ) of around 0.95 - 0.99, meaning that the correction needed for the presence of multiply-charged ion species results in a decrease of the anode efficiency by 1 to 5%;
- The neutral-gain factor ( $\varepsilon_{NG}$ ) of the Ex-Halo thruster remains below 1.08 at almost all the conditions surveyed - except for the thruster operative point at 150 V, at which the ionization is reduced, yielding a higher contribution of the neutral flow momentum (the mass utilization efficiency at 150 V is between 0.15 and 0.45);
- The voltage utilization efficiency ( $\eta_v$ ) spans from 0.78 to 0.87 for almost all the Ex-Halo conditions here surveyed;
- The beam utilization efficiency ( $\eta_{div}$ ) ranges between 0.55 and 0.75 and highlights the performance losses due to the plume divergence angle;
- The Int-Halo shows higher values of mass utilization efficiency ( $\eta_m$ ) - in the low-voltage range (150 V – 200 V) at all the mass flow rates surveyed - in comparison to the Ex-Halo configuration. Nevertheless, the operative conditions of the Int-Halo correspond to a higher thruster power range;

- The Int-Halo features low current utilization efficiency ( $\eta_b = 0.15 - 0.25$ ) as the electron current represents the majority of the discharge current. This also causes an undesirable overheating of the anode which limits thruster operations to low mass flow rates and voltage levels;
- The Int-Halo features a charge utilization efficiency ( $\eta_q$ ) of around 0.96 - 0.99, meaning that correction accounting for the presence of multiply-charged ion species results in a decrease of the anode efficiency by 1 to 4%;
- The Int-Halo neutral-gain factor ( $\epsilon_{NG}$ ) remains below 1.05 at all the conditions surveyed;
- The Int-Halo voltage utilization efficiency ( $\eta_V$ ) spans from 0.7 to 0.85;
- The beam utilization efficiency ( $\eta_{div}$ ) is around 0.65.

To highlight which loss mechanisms exhibit the most severe contribution, Figs. 12 and 13 plot the utilization efficiencies of the Ex-Halo at 0.98 mg/s and 1.47 mg/s, respectively. Similar patterns are observed at 1.97 mg/s and therefore it is not reported in the following.

The efficiency plots highlight that improvements of the Ex-Halo design must focus primarily on the increase of the mass and current utilization efficiencies at low voltage levels. The low value of  $\eta_m$  demonstrates that a large fraction of propellant injected through the anode is not ionized. This is further highlighted by a low  $\eta_b$ , which indicates that electrons are not efficiently used to ionize the propellant. Electrons are reaching more easily the anode, escaping via the magnetic null regions in front of the anode. The thruster operates at higher current for the same voltage and mass flow rate for the Int-Halo configuration versus the Ex-Halo. High plasma density profiles previously measured in CHT plumes suggest that, nominally, these devices are quite efficient in terms of ion production [87, 88]. Therefore, this result was unforeseen when the Halo thruster was originally designed.

A breakdown of the Ex-Halo discharge power into  $P_{ion-beam}$ ,  $P_{min}$  and  $P_{loss}$  for the different mass flow rates and anode voltages is shown in Fig. 14. The  $P_{ion-beam}$  is evaluated

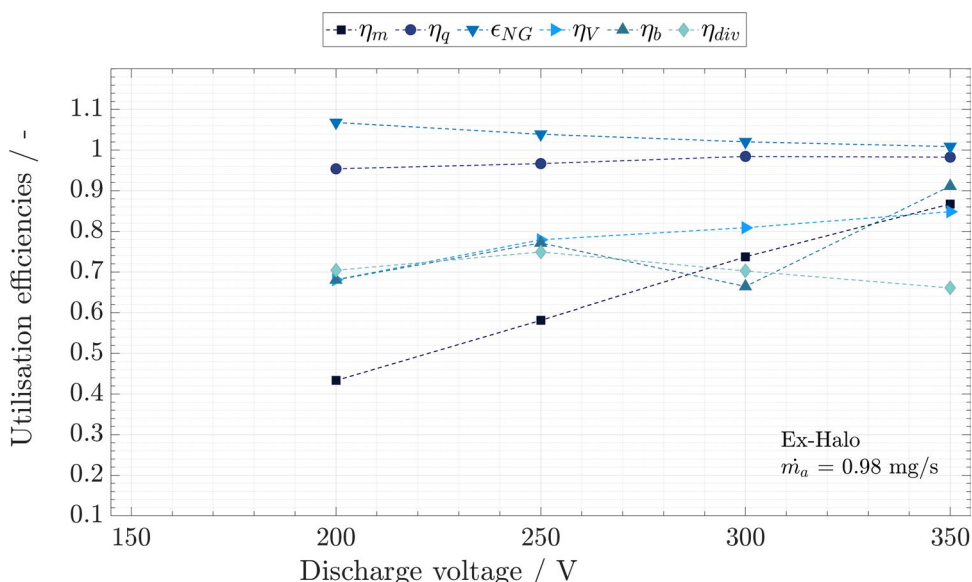


**Fig. 12** Utilization efficiencies as a function of the discharge voltage: EX-Halo at 0.98 mg/s

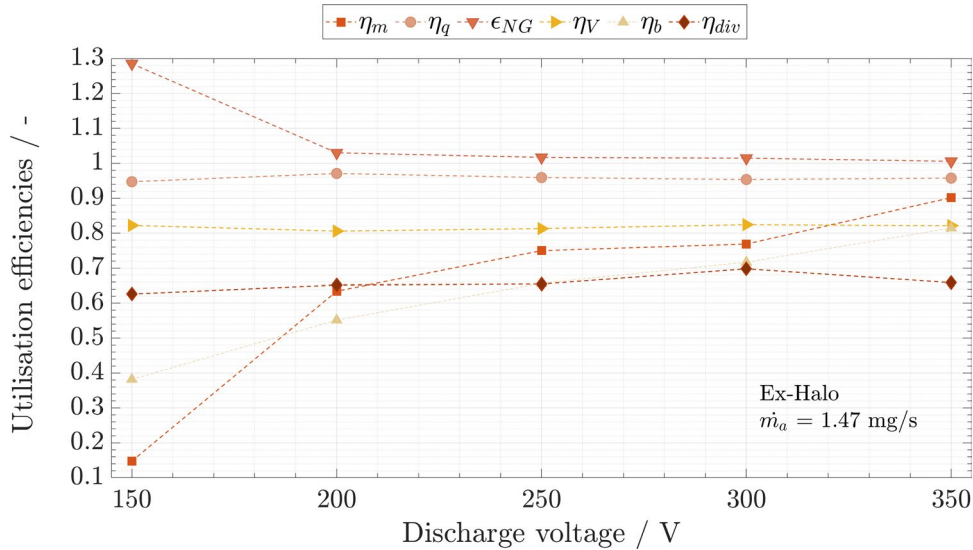


**Fig. 13** Utilization efficiencies as a function of the discharge voltage: EX-Halo at 1.47 mg/s

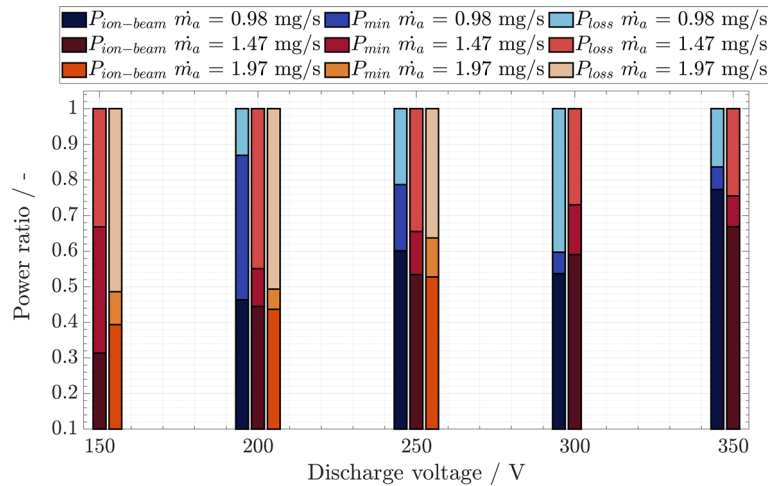


**Fig. 14** Breakdown of the Ex-Halo discharge power into  $P_{\text{ion-beam}}$ ,  $P_{\text{min}}$ , and  $P_{\text{loss}}$ . The  $P_{\text{ion-beam}}$  is the product of the most probable acceleration voltage and the ion beam current. Blue bars are indicative of  $\dot{m}_a = 0.98 \text{ mg/s}$ , red bars of  $\dot{m}_a = 1.47 \text{ mg/s}$  and orange bars of  $\dot{m}_a = 1.97 \text{ mg/s}$

as the product of the most probable acceleration voltage measured by the Wien filter and the ion beam current measured by the Faraday probe. It does not include divergence losses and is the overall power on a hemispherical surface. As radial losses are significant, they drastically reduce the fraction of this power that is linked to the production of useful axial thrust. The  $P_{\text{min}}$  is the minimum power required to generate the ion species and is evaluated as Eq. 21 and  $P_{\text{loss}}$  is the power lost by Joule heating and wall losses estimated as in Eq. 23.  $P_{\text{loss}}$  and  $P_{\text{min}}$  are intrinsically related as the more power is lost to the walls, the colder the plasma and the lesser energy is available for ionization of the ion species. By analyzing plasma measurements performed within the EM Halo discharge channel by Wantock [89], it can be noticed that a region of high electron density was observed near the channel walls where the cusped B-field lines intersect the ceramic surface. This high electron density region does not characterize CHTs of similar size and

different magnetic field topology [90]. It may be suggested that the peculiar B-field of the Halo thruster facilitates electron transport to the walls and contributes to the high  $P_{loss}$  here measured. At greater discharge voltages,  $P_{ion-beam}$  increases and less power is lost to the wall or is used to sustain the plasma. As suggested by the utilization efficiency plots (Figs. 12 and 13), this is the result of more efficient use of voltage and current. A larger electric field results in hotter electrons, as well as stronger acceleration. The charge utilization and the ion beam divergence efficiencies remain almost constant within the voltage range surveyed. However, attempts to decrease the divergence of the beam should be made to mitigate losses and increase the overall efficiency. The neutral-gain parameter is linked to the mass and charge utilization efficiencies and does not introduce major impacts on the conclusions since its value remains close to 1.

Figure 15 shows the utilization efficiencies of the Int-Halo configuration at 0.49 mg/s. Despite only a few data points being available for the Int-Halo configuration, the data are still useful to understand the loss mechanisms for this thruster configuration. The low efficiency of the Int-Halo thruster is predominantly determined by the low current utilization efficiency. As Fig. 16 confirms, most of the discharge power is lost in Joule heating and wall losses and below 20% goes into the ion beam. In addition, this is the overall ion beam power fraction in an hemispherical surface, without accounting for divergence effects that drastically decrease the useful (i.e., axial) beam power linked to the generation of axial thrust. Taking this additional effect into account, the overall efficiency of this configuration is typically below 10%. This explains the more rapid temperature increment in comparison to the Ex-Halo configuration and the overheating and melting issues of the anode experiences during the test campaign. Similarly to the Ex-Halo design, at low voltage levels only around 50% of the anode propellant is ionized. The voltage utilization efficiency can be considered comparable, or even greater. Finally, beam divergence and charge utilization efficiencies are similar in the two configurations.

### B. Halo thruster semi-empirical model

The model presented in Sec. B has been refined based on the utilization efficiency data of the Ex-Halo thruster. As already demonstrated by Shagayda [14] and in line with the

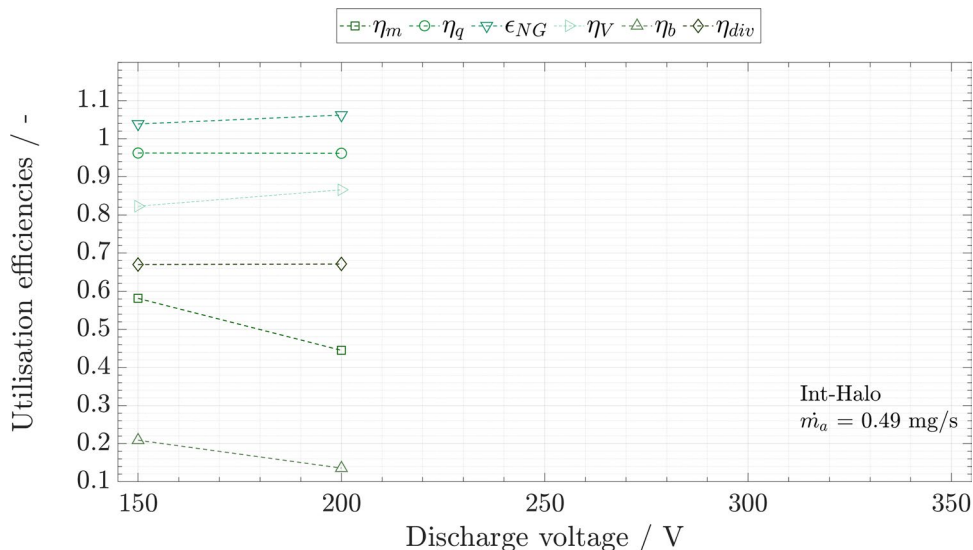


**Fig. 15** Utilization efficiencies as a function of the discharge voltage: Int-Halo at 0.49 mg/s

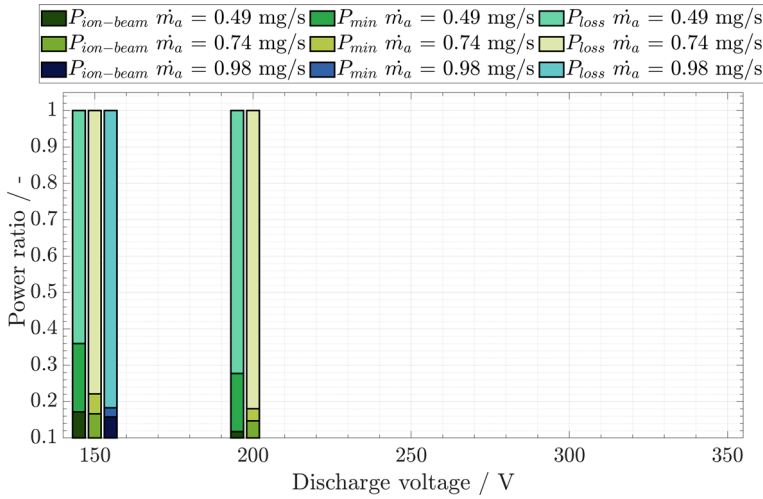


**Fig. 16** Breakdown of the Int-Halo discharge power into  $P_{ion-beam}$ ,  $P_{min}$  and  $P_{loss}$ . Dark green bars are indicative of  $\dot{m}_a = 0.49 \text{ mg/s}$ , light green bars of  $\dot{m}_a = 0.74 \text{ mg/s}$  and blue bars of  $\dot{m}_a = 0.98 \text{ mg/s}$ .  $P_{ion-beam}$  is the overall ion beam power fraction in an hemispherical surface, without accounting for divergence effects that drastically decrease the useful (i.e., axial) beam power linked to the generation of axial thrust

Ex-Halo experimental data, the mass utilization efficiency depends on the thruster operative points and the voltage utilization efficiency can be approximated as a constant. Differently from the reference model in which  $\eta_b$  is taken as a constant and according to the Ex-Halo empirical data, a trend between the current utilization efficiency and the thruster discharge power can be observed. This trend can be approximated as a second-degree polynomial function. The charge utilization efficiency is nearly constant for all the Ex-Halo operative points here surveyed and the multiply charged ions flow fractions are quite well approximated by first-degree polynomial functions. In summary, the conditions identified for the Halo thruster predictive model are the following:

- $\eta_v^*(Ex-Halo)$  is defined as a constant value and, based on the Ex-Halo experimental data, is set equal to 0.52 taking into account the voltage utilization efficiency and beam divergence efficiency;
- the charge utilization efficiency is found to be almost constant for all the Ex-Halo thruster operative points here surveyed and determined equal to  $\eta_q(Ex-Halo) = 0.96$ ;
- the ion flow fractions are approximated as linear functions of the discharge power as in Eqs. 36 - 38:

$$\mu_{Xe^+} = \Gamma_1 \cdot P_d + 0.8221; \quad (36)$$

$$\mu_{Xe^{+2}} = \Gamma_2 \cdot P_d + 1.292; \quad (37)$$

$$\mu_{Xe^{+3}} = 1 - \mu_{Xe^+} - \mu_{Xe^{+2}} \quad (38)$$

where  $\Gamma_1$  and  $\Gamma_2$  are dimensional constants. Their values are, respectively,  $\Gamma_1 = -0.0004 \text{ W}^{-1}$  and  $\Gamma_2 = 0.0003 \text{ W}^{-1}$ ;

- the current utilization efficiency is defined as a function of the discharge voltage and evaluated as the curve that approximates the empirical data using a least squared method (Eq. 39):

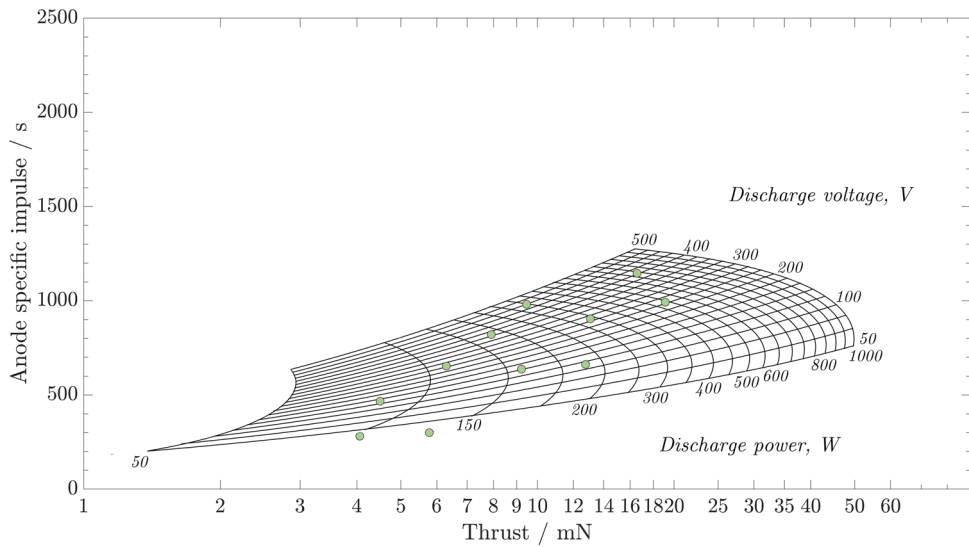


**Fig. 17** Estimated Halo anode specific impulse as a function of the Halo thrust at different discharge powers and discharge voltages. Experimental data of the ex-Halo [83, 85] are superimposed on the data lines

$$\eta_{b(Ex-Halo)} = \beta_1 \cdot V_d^2 + \beta_2 \cdot V_d - 0.019 \quad (39)$$

where  $\beta_1$  and  $\beta_2$  are dimensional constants. Their values are  $\beta_1 = -3 \cdot 10^{-6} \text{ V}^{-2}$  and  $\beta_2 = 3.5 \cdot 10^{-3} \text{ V}^{-1}$ ;

- the mass utilization efficiency is evaluated as in Eq. 31, assuming a proportional relation between electron temperature and discharge voltage as in Eq. 35 and  $C_{Te(Ex-Halo)} = 0.07$ .

The performance diagram in Fig. 17 illustrates the predicted performance envelope in the plane anode specific impulse (evaluated as in Eq. 29)/ thrust (calculated according to Eq. 28). The plot is the superimposition of two sets of curves: one group corresponds to a change in the discharge voltage for fixed values of discharge power ranging between 50 W and 1000 W; the other group compares the change in discharge power for fixed discharge voltage data spanning from 50 V to 500 V. The discharge voltage and power values are shown close to the curves. The experimental data of the Ex-Halo thruster [83, 85] are also plotted as green circles.

Figure 17 shows that the semi-empirical performance model is able to predict the empirical data with a certain margin of error. Although the experimental performance data points are broadly within the overall predicted performance envelop, the model does not necessarily capture the correct operating conditions (anode voltage and power) of their occurrence. Nevertheless, given that the performance values of the Halo thruster are quite dissimilar from the majority of the experimental points included in the database in Sec. A (including data from CHTs and CFTs), the refinement of the semiempirical model had to rely on Halo empirical data of this work only, otherwise, the inclusion of other thrusters' data points could yield to an overestimation of the Halo's performance. This is quite unfortunate since semi-empirical methodologies rely on a data library and their predictive value depends on the available experimental test results.

Figure 17 is useful to determine the range of power level and the discharge voltage necessary to reach the required Halo thruster performance. It also highlights that quite a broad range of anode specific impulse and thrust levels has already been surveyed

during experimental tests and shows the limited margin of improvement of the current Ex-Halo design.

### Conclusions

This work has introduced a phenomenological Hall thruster performance model derived as function of utilization efficiencies and has detailed a semi-empirical method to predict the performance of Hall-based thrusters working at a maximum power level of 1 kW. The phenomenological model separates the total thruster efficiency into six efficiency terms: charge utilization, mass utilization, current utilization, voltage utilization efficiencies and two factors that are representative of the divergence in the ion beam and the effects of neutrals in the jet velocity distribution. The main thruster performance parameters can be expressed in terms of these utilization efficiencies and be used as the basis of a semi-empirical model. The semi-empirical model here proposed is a continuation of Shagayda's work on HETs working with different propellants. The methodology has been tailored to experimental data of around sixty HETs, including novel designs such as CHTs, CFTs and MS-HETs. The aim of the proposed model is to predict the performance of Hall-based thrusters operating at power levels up to 1 kW and using xenon as the propellant. Ultimately, the methodology is used to forecast the Halo thruster performance. The efficiency analysis is used to analyze the ionization, acceleration and loss mechanisms in the Halo thruster discharge. Despite a similar design, the two Halo thruster configurations - with internal and external HCN - are governed by different plasma behaviors. The performance losses in the Ex-Halo are mostly related to the low ionization rate and low mass utilization efficiency. In the Int-Halo, these loss mechanisms are even more significant, especially the very low current utilization efficiency and the power lost due to heating and wall losses, which make almost impossible to operate the thruster without excessive overheating. Comparing the two thruster designs, the Int-Halo configuration showed lower performance since electrons find an easier path towards the anode without promoting sufficient ionization and, conversely, increasing power losses and causing overheating of the system. The most likely explanation for the unusually high temperature is the Halo thruster magnetic field topology, which funnels a large number of electrons from the central cathode towards the anode through a preferential path via the toroidal magnetic null region.

### Appendix

**Table A** List of the thruster data (model, discharge voltage range and power range) used to compile the dataset comprising < 1 kW hall effect based thrusters. The references numbers of the sources of data for each thruster are reported in the text of Sec. A

Thruster	Manufacturer	Model	Discharge Voltage [V]	Power [W]
KM-20	Keldysh Research Centre	HET	350	210
KM-32	Keldysh Research Centre	HET	200 - 400	90 - 390
KM-45	Keldysh Research Centre	HET	310 - 320	275 - 400
KM-60	Keldysh Research Centre	HET	500	900
SPT-30	Fakel	HET	100 - 250	90 - 260
<i>a</i> -40 SPT	Fakel	HET	150 - 210	95 - 185
SPT-50	Fakel	HET	150 - 400	75 - 370
SPT-70	Fakel	HET		650 - 700
T40 HTC	Fakel	HET	150 - 300	115 - 240

**Table A** List of the thruster data (model, discharge voltage range and power range) used to compile the dataset comprising < 1 kW hall effect based thrusters. The references numbers of the sources of data for each thruster are reported in the text of Sec. A

Thruster	Manufacturer	Model	Discharge Voltage [V]	Power [W]
Plas-34	Fakel	HET	120 - 300	150 - 375
Plas-40	Fakel	HET	100 - 450	125 - 610
D-38	TSNIIMASH	HET	100 - 300	75 - 300
T-27	TSNIIMASH	HET	120 - 300	65 - 300
BHT-100	Busek	HET	200	100
BHT-200	Busek	HET	225 - 300	200
BHT-600	Busek	HET	300	600 - 650
BHT-1000	Busek	HET	100 - 450	200 - 1000
MaSMI-40	NASA	HET		320
MaSMI-60	NASA	HET	200 - 400	160 - 750
micro HET	Stanford University	HET	200 - 255	25 - 30
Z70	Stanford University	HET	200 - 300	350 - 590
Aurora HET	Orbion Space Technology	HET		100 - 300
ACE	Astra	HET		320
Halo	Exoterra	HET		60 - 310
Mini SPT	MIT	HET	200 - 300	20 - 130
DCFT	MIT	CFT		60 - 215
CHT 9	PPPL	CHT	200 - 300	300 - 820
CHT 2.6	PPL	CHT	200 - 300	85 - 325
CHT 3	PPPL	CHT	250 - 350	90 - 180
OEFT	ASRI	wall-less HET	400 - 1200	0.6 - 6
CAM200	ASRI	co-axial HET	200 - 275	100 - 300
CAMILA	ASRI	co-axial HET	250 - 300	150 - 300
IHET-300	Rafael	HET		275 - 540
NCHT	Rafael	narrow channel HET	65 - 100	20 - 40
R-200	Rafael	HET		150 - 350
R-800	Rafael	HET		450 - 900
HEET	LAJP	HET		100 - 720
SPT-20 M	SETS	HET		50 - 92
ST-25	SETS	HET	160 - 240	80 - 215
ST-40	SETS	HET	180 - 280	150 - 450
SHT 100	Seran	HET	200	100
SHT 250	Seran	HET	250	210
ISCT-100	CNRS	HET	200 - 350	70 - 200
ISCT-200-US	CNRS	HET	150 - 300	110 - 350
ISCT-200-MS	CNRS	HET	150 - 300	150 - 325
ExoMG	ExoTrail	HET		40 - 1000
HT100	Alta	HET	175 - 400	170 - 355
50 W-class HET	KAIST	HET	160 - 280	40 - 75
300 W-class HET	KAIST	HET	175 - 500	150 - 500
KCHT-50	KAIST	CHT	200 - 350	180 - 330
KmCHT50	KAIST	CHT	200 - 350	190 - 340
CHT 5	KAIST	CHT	200 - 380	210 - 350
CHT 4	KAIST	CHT	210	110 - 150
100 W-class HET	JAXA	HET	150 - 300	80 - 100
TCHT-3A	Osaka University	CHT		130 - 310
TCHT-3B	Osaka University	CHT	200	150 - 200
TCHT-4	Osaka University	CHT	100 - 350	15 - 275
CHT 1.4	Osaka University	CHT	100 - 300	10 - 240
CHT 5.6	Osaka University	CHT	200	300 - 425
MUSIC Si	Aliena	HET		7.5 - 16

**Table A** List of the thruster data (model, discharge voltage range and power range) used to compile the dataset comprising < 1 kW hall effect based thrusters. The references numbers of the sources of data for each thruster are reported in the text of Sec. A

Thruster	Manufacturer	Model	Discharge Voltage [V]	Power [W]
MUSIC HM	Aliena	HET		130 - 185
CHT	Harbin Institute of Technology	CHT	150 - 350	65 - 200
CHT PM	Harbin Institute of Technology	CHT	100 - 200	50 - 120
HEMPT	Thales Germany	CFT		200 - 700
Ex-Halo	SSC/Airbus	CHT	150 - 350	70 - 850

#### Acknowledgements

The Halo thruster research and development activities were supported by Airbus Defence & Space and the UK Space Agency under the "Development of a Halo-200 Electric Propulsion System" project. Gratitude is extended to Surrey Satellite Technology Limited (SSTL) for the PhD studentship, which has provided essential support for this work and has facilitated various opportunities for growth and learning throughout the research journey.

#### Author contributions

S. M: Investigation (lead); Conceptualization (equal); Methodology (lead); Software (lead); Tests (lead); Validation (lead); writing—original draft (lead). A. LF: Conceptualization (equal); Formal analysis (lead); Funding acquisition (lead); Supervision (lead). P.B: Conceptualization; Funding acquisition.

#### Data availability

Raw data were generated at Surrey Space Centre (SSC), University of Surrey. Derived data supporting the findings of this study are available from the corresponding author S.M. on request.

#### Declarations

##### Competing interests

The authors declare no competing interests.

Received: 31 March 2025 / Accepted: 12 October 2025

Published online: 07 November 2025

#### References

- Choueiri EY (2004) A critical history of electric propulsion: the first 50 years (1906–1956). *J Propul Power* 20(2):193–203
- Lev D et al (2019) The technological and commercial expansion of electric propulsion. *Acta Astronautica* 159:213–227
- Komurasaki K, Arakawa Y (1992) Hall current ion-thruster performance. *J Propul Power* 8(6):1212–1216
- Kim V (1998) Main physical features and processes determining the performance of stationary plasma thrusters. *J Propul Power* 14(5):736–743
- Bugrova AI et al (2005) Effect of the ratio of differently charged ions on the integral parameters of stationary plasma thrusters of the aton type. *Tech Phys Lett* 31(11):943–946
- Bugrova AI et al (2002) On a similarity criterion for plasma accelerators of the stationary plasma thruster type. *Tech Phys Lett* 28(10):821–823
- Bouchoule A et al (2004) Physical investigations and developments of hall plasma thrusters. *Plasma Phys Control Fusion* 46(12B):B407
- Biagioni L, Saverdi M, Andrenucci M (2003) Scaling and performance prediction of hall effect thrusters. In 39th AIAA/ASME/SAE/ASEE Joint Propulsion Conference and Exhibit, pp 4727
- Linnell JA, Gallimore AD (2006) Efficiency analysis of a hall thruster operating with krypton and xenon. *J Propul Power* 22(6):1402–1418
- Ahedo E, Gallardo JM, Martínez-Sánchez M (2002) Model of the plasma discharge in a hall thruster with heat conduction. *Phys Plasmas* 9(9):4061–4070
- Hofer RR, Gallimore AD (2006) High-specific impulse hall thrusters, part 2: efficiency analysis. *J Propul Power* 22(4):732–740
- Hofer R, Jankovsky R (2001) A hall thruster performance model incorporating the effects of a multiply-charged plasma. In 37th Joint Propulsion Conference and Exhibit, pp 3322
- Brown DL et al (2009) Methodology and historical perspective of a hall thruster efficiency analysis. *J Propul Power* 25(6):1163–1177
- Shagayda AA (2014) On scaling of hall effect thrusters. *IEEE Trans Plasma Sci* 43(1):12–28
- Murashko V et al (2003) State of the art and prospects of electric propulsion in Russia. In 28th International Electric Propulsion Conference, Toulouse, France
- Gorshkov DO, Shagayda DA, Muravlev MV (2006) The experience of hall thruster research and development. In: 57th Int Astronaut Congr. C4–4
- Szabo J, Azziz Y (2005) Characterization of a high specific impulse xenon hall effect thruster. In 29th International Electric Propulsion Conference, Princeton University
- Peterson P et al (2007) Hall thruster technology for nasa science missions: HiVHAC status update. In 43rd AIAA/ASME/SAE/ASEE Joint Propulsion Conference & Exhibit, pp 5236
- Duchemin O et al (2003) Development and testing of a high-power hall thruster. In Proceedings of the 28th International Electric Propulsion Conference, Toulouse, France

20. Ozaki T et al (2005) Development status of 200mN class xenon hall thruster of melco. In Proc. 29th International Electric Propulsion Conference, Citeseer, Princeton, USA, IEPC2005–064
21. Dignani D et al (2011) HT-100 hall thruster characterization tests results. In IEPC 32nd International Electric Propulsion Conference, Wiesbaden, Germany
22. Goebel DM, Katz I (2008) Fundamentals of electric propulsion: ion and hall thrusters. John Wiley & Sons
23. Gorshkov OA, Shagayda AA (2008) Determining the efficiency of a plasma thruster with closed electron drift. *Tech Phys Lett* 34(2):153–155
24. Hofer R, Gallimore A (2004) Efficiency analysis of a high-specific impulse hall thruster. In 40th AIAA/ASME/SAE/ASEE Joint Propulsion Conference and Exhibit, pp 3602
25. Bugrova AI et al (2001) Design and experimental investigation of a small closed drift thruster. In Proceedings of the International Electric Propulsion Conference, USA, Pasadena, CA, 15–19
26. Belikov M et al (2007 September 17–20) Development of low-power hall thruster with lifetime up to 3000 hours. In iepc-2007-129, 30th Int Electric Propul Conf, Florence, Italy
27. Gorshkov OA et al (2008) The GEOSAT electrical propulsion subsystem based on the KM-45 het. *Acta Astronautica* 63:367–378. 1–4
28. Jacobson D, Jankovsky R (1998) Test results of a 200W class hall thruster. In 34th AIAA/ASME/SAE/ASEE Joint Propulsion Conference and Exhibit, pp 3792
29. Manzella D et al (1996) Evaluation of low power hall thruster propulsion. In 32nd Joint Propulsion Conference and Exhibit, pp 2736
30. Frieman JD et al (2016) Performance evaluation of the T-40 low-power hall current thruster. In 52nd AIAA/SAE/ASEE Joint Propulsion Conference, pp 4833
31. Yu Bernikova M, Gopanchuk. VV (2017) Parametric family of the PlaS-type thrusters: development status and future activities. In 35th International Electric Propulsion Conference, Georgia Institute of Technology, USA, Atlanta, Georgia, 8–12
32. M et al (1998) Experimental research of spt low-power perspective model. In 34th AIAA/ASME/SAE/ASEE Joint Propulsion Conference and Exhibit, pp 3786
33. Zakharenkov L et al (2001) Study of low power tal characteristics. In 27-th International Electric Propulsion Conference.– Pasadena USA, 2001, USA,–IEPC-01. 41
34. Szabo JJ et al (2017) Characterization of a one hundred watt, long lifetime hall effect thruster for small spacecraft. In 53rd AIAA/SAE/ASEE Joint Propulsion Conference, pp 4728
35. Ekholm J, Hargus W (2005) E x B measurements of a 200 W xenon hall thruster. In 41st AIAA/ASME/SAE/ASEE Joint Propulsion Conference & Exhibit, pp 4405
36. Azziz Y, Martinez-Sanchez M (2003) Plasma measurements on a 200-watt hall thruster plume. In Proceedings of the 28th International Electric Propulsion Conference, Toulouse, France
37. Nakles MR et al (2009) A plume comparison of xenon and krypton propellant on a 600 W hall thruster. Tech. rep. Air force research lab Edwards AFB CA propulsion Directorate
38. Pote B, Tedrake R (2001) Performance of a high specific impulse hall thruster. In Proceedings of the 27th International Electric Propulsion Conference, Pasadena, CA, 01–035
39. Conversano RW et al (2017) Performance enhancement of a long-life, low-power hall thruster for deepspace smallsats. In 2017 IEEE Aerospace Conference, IEEE, pp. 1–12
40. Conversano RW (2015) Low-power magnetically shielded hall thrusters. PhD thesis. University of California, Los Angeles
41. Ito T et al (2007) Experimental characterization of a micro-hall thruster. *J Propul Power* 23(5):1068–1074
42. Marcovati A (2016) Z-70 hall thruster performance analysis. Experimental thrust and plasma measurements. PhD thesis
43. Sommerville JD et al (2019) Performance of the Aurora low-power hall-effect thruster. In Proceedings of the 36th International Electric Propulsion Conference, Vienna, Austria. 15–20
44. Gill M et al (2022) On-orbit data and validation of Astra's ace electric propulsion system. In
45. VanWoerkom M et al (2019) Test results of exoterra's Halo micro electric propulsion system for microsatellites. AIAA Propul And Energy 2019 Forum. 4163
46. Daspit RM (2012) Performance characterization and optimization of a diverging cusped field thruster with a calibrated counter-weighted millinewton thrust stand. PhD thesis. Massachusetts Institute of Technology
47. Polzin KA et al (2007) Performance of a low-power cylindrical hall thruster. *J Propul Power* 23(4):886–888
48. Raitses Y, Fisch NJ (2001) Parametric investigations of a nonconventional hall thruster. *Phys Plasmas* 8(5):2579–2586
49. Smirnov A, Raitses Y, Fisch NJ (2007) Experimental and theoretical studies of cylindrical hall thrusters. *Phys Plasmas* 14(5), p. 057106
50. Smirnov A, Raitses Y, Fisch NJ (2002) Parametric investigation of miniaturized cylindrical and annular hall thrusters. *J Appl Phys* 92(10):5673–5679
51. Hamo O et al (2022) Experimental investigation of an external discharge very low anode power (< 20 W) hall thruster. *J Educ Chang Electric Propul* 1(1):16
52. Lev D et al (2016) The development of CAM200-low power hall thruster. *Trans Of The Jpn Soc For Aeronaut And Space Sci, Aerosp Technol Jpn* 14(ists30):b\_217–Pb\_223
53. Kapulkina A et al (2011) Camila hall thruster: new results. In Proceedings of the 32nd International Electric Propulsion Conference (IEPC), pp 11–15
54. Kronhaus I, Linossier A (2018) Experimental characterization of the narrow channel hall thruster. *Plasma Sources Sci Technol* 27(12), p. 124005
55. Shoor B et al (2019) The Rafael power processing unit (ppu) for electric propulsion systems. In International Electric Propulsion Conference, University of Vienna, Austria
56. Petrenko O et al (2020) Hall thruster ST-25 developed by space electric thruster system (sets). In Space Propulsion Conference
57. Hallouin T et al (2019) Far-field plume diagnostic of the 100 W-class ISCT100-v2 hall thruster. In Proceedings of the 36th International Electric Propulsion Conference, University of Vienna, Wien, Austria, 15–20
58. Grimaud L, Mazouffre S (2018) Performance comparison between standard and magnetically shielded 200 W hall thrusters with BN-SiO<sub>2</sub> and graphite channel walls. *Vacuum* 155:514–523

59. Gurciullo A et al (2019) Experimental performance and plume characterisation of a miniaturised 50W hall thruster. In 36th International Electric Propulsion Conference, University of Vienna, Austria
60. Ducci C et al (2013) HT100D performance evaluation and endurance test results. In Proceedings of the 33rd International Electric Propulsion Conference, Washington, DC, USA, 6–10
61. Lee D et al (2019) Development and performance test of a 50 W-class hall thruster. In 36th International Electric Propulsion Conference (University of Vienna, Vienna, Austria, 15–20)
62. Lee D et al (2021) Distinct discharge modes in micro hall thruster plasmas. *Plasma Sources Sci Technol* 30(3), p. 035004
63. Kim Y et al Performance comparison of xenon and krypton discharges in a 300 W-class hall thruster. In Proceedings of the International Electric Propulsion Conference, Massachusetts Institute of Technology, Cambridge, MA USA, USA, 2022
64. Kim H et al (2014) Effect of multiply charged ions on the performance and beam characteristics in annular and cylindrical type hall thruster plasmas. *Appl Phys Lett* 105(14), p. 144104
65. Kim H et al (2017) Magnetic field configurations on thruster performance in accordance with ion beam characteristics in cylindrical hall thruster plasmas. *Appl Phys Lett* 110(11), p. 114101
66. Watanabe H, Cho S, Kubota K (2019) Performance evaluation of a 100-W class hall thruster. In Proceedings of the 36th International Electric Propulsion Conference, University of Vienna, Wien, Austria, 15–20
67. Watanabe H, Cho S, Kubota K (2020) Performance and plume characteristics of an 85 W class hall thruster. *Acta Astronautica* 166:227–237
68. Shirasaki A, Tahara H (2005) Plume measurements and miniaturization of the hall thrusters with circular cross-sectional discharge chambers. In 29th International Electric Propulsion Conference, pp 2005–2051
69. Ikeda T et al (2013) Performance characteristics of very low power cylindrical hall thrusters for the nano-satellite "PROITERES-3". *Vacuum* 88:63–69
70. Laterza M et al (2022) Multi-stage ignition compact thruster concept and testing. In Proceedings of the 37th International Electric Propulsion Conference, Cambridge. EPC-2022–294
71. Yongjie D et al (2017) A type of cylindrical hall thruster with a magnetically insulated anode. *J Phys D: Appl Phys* 50(14), p. 145203
72. Ding Y et al (2018) Comparative study of annular-cylindrical combined channel with annular channel hall thruster. *IEEE Trans Plasma Sci* 46(12):4051–4059
73. Gao Y et al (2020) Influence of near-anode cusped magnetic field on the performance of a miniaturized cylindrical hall thruster. *Plasma Sources Sci Technol* 29(9), p. 095021
74. Heidemann R et al (2019) Development of the low power HEMPT EV0. In Proceedings of the 36th International Electric Propulsion Conference, Vienna, Austria, IEPC–2019–A873
75. Hofer R, Gallimore A (2003) Ion species fractions in the far-field plume of a high-specific impulse hall thruster. In 39th AIAA/ASME/SAE/ASEE Joint Propulsion Conference & Exhibit, pp 7014
76. King LB, Gallimore AD (2000) Ion-energy diagnostics in the plasma exhaust plume of a hall thruster. *J Propul Power* 16(5):916–922
77. Shagayda AA, Gorshkov OA (2013) Hall-thruster scaling laws. *J Propul Power* 29(2):466–474
78. Dannenmayer K, Mazouffre S (2011) Elementary scaling relations for hall effect thrusters. *J Propul Power* 27(1):236–245
79. Raitses Y et al (2005) The dependence of the electron temperature on the discharge voltage for different hall thruster configurations. In Proceedings of the 29th Int. Electric Propulsion Conference–Princeton (USA), 2005. p 8. (Paper 2005-52)
80. Hofer R (2010) High-specific impulse operation of the BPT-4000 hall thruster for nasa science missions. In 46th AIAA/ ASME/SAE/ASEE Joint Propulsion Conference & Exhibit, pp 6623
81. Meeker D Finite element method magnetics. <https://www.femm.info/>. (Accessed: 06.02.2023)
82. Karadag B et al (2019) Experimental investigation and performance optimization of the Halo thruster. In 36th International Electric Propulsion Conference (IEPC)
83. Masillo S et al (2021) Experimental characterisation of the novel Halo plasma thruster for small satellite applications. In Proceedings of the 7th Space Propulsion Conference
84. Masillo S et al (2022) Validation of a torsional balance for thrust measurements of hall effect and microwavebased space propulsion systems. *Rev Sci Instrum* 93(11):114501
85. Masillo S (2023) Experimental characterisation of a novel hall-type plasma thruster for small satellite applications. PhD thesis
86. Ahmed M et al (2024) Development of a modular hollow cathode for ground testing of plasma thrusters. *Vacuum* 219: 112653
87. Smirnov A, Raitses Y, Fisch NJ (2004) Plasma measurements in a 100 W cylindrical hall thruster. *J Appl Phys* 95(5):2283–2292
88. Perrotin T et al (2022) Characterization of a low-power cylindrical hall thruster. In 37th International Electric Propulsion Conference
89. Wantock TG (2017) Thrust balance performance characterisation and internal Langmuir probe plasma diagnostics for a Halo thruster. University of Surrey. United Kingdom
90. Diamant K et al (2008) Low power cylindrical hall thruster performance and plume properties. In 44th AIAA/ASME/SAE/ ASEEE Joint Propulsion Conference & Exhibit, pp 4998

## Publisher's Note

Springer Nature remains neutral with regard to jurisdictional claims in published maps and institutional affiliations.